A Novel Approach for In-Orbit Satellite Antenna Pattern Measurement using a Small Satellite Flying in Double-Cross-Helix Formation

Josef Mittermayer, Gerhard Krieger, *Fellow, IEEE*, and Michelangelo Villano, *Senior Member, IEEE*

Abstract — The paper proposes a novel approach for in-orbit satellite antenna pattern measurement by means of a dedicated small measurement satellite that flies in Double-Cross-Helix formation. For establishing and maintaining the quality of a satellite mission and its products, antenna pattern measurement while the satellite is in orbit is crucial. In remote sensing missions like Synthetic Aperture Radar (SAR), the pattern is measured using calibration targets on the Earth's surface. Such on-ground measurements are costly, time-consuming, and only offer one-dimensional azimuth or elevation patterns within constrained angular ranges. The novel approach provides a two-dimensional in-orbit measurement that covers the full angular range. The two-dimensional pattern is obtained from numerous central cuts resulting from small modifications of the measurement satellite's orbit parameters that establish the Double-Cross-Helix formation. The measurement is performed in free space with a single free-flying measurement satellite. This avoids all distortions from atmosphere, ionosphere, ground clutter and multipath effects, ambiguities, and volume scattering. The approach is of great value for future satellite missions that are increasingly based on a huge number of electronically steered antenna beams and/or digital beamforming. The Dual-Cross-Helix approach provides faster, cheaper, and more accurate pattern measurements. The paper discusses a high-level system concept of a feasible in-orbit pattern measurement of a SAR satellite similar to TerraSAR-X by means of a passive measurement satellite that is equipped with a reflecting sphere. Orbit simulations, measurement gain and angular sampling accuracy analyses verify that the Double-Cross-Helix approach is feasible and advantageous for in-orbit antenna pattern measurement.

Index Terms—In-Orbit Antenna Pattern Measurement, Satellite Formation, Double-Cross-Helix, Reflecting Sphere.

I. INTRODUCTION

In the course of a radar satellite mission, an up-to-date knowledge of the antenna pattern is a precondition for establishing and maintaining the mission product quality. The antenna pattern is usually measured pre-launch - fully for small satellites and often only partially in case of large antennas.

However, due to launch, antenna un-folding in space, hardware and structure aging or failure, the antenna pattern alters constantly during the mission. Therefore, the pattern is required to be measured again after launch as part of the commissioning phase, e.g. [1]-[2], and then repeatedly at regular intervals during the operational phase.

For radar satellites in Low Earth Orbiting (LEO) orbits, the post-launch antenna pattern measurements are based on on-ground calibration targets and calibration test sites. This is expensive and time consuming since effortful on-ground campaigns have to be carried out. The on-ground measurements are limited in accuracy, and cannot provide individual transmit (Tx) and receive (Rx) patterns over wide angle-ranges. Only azimuth or range patterns can be measured, which are one-dimensional cuts through the two-dimensional antenna pattern in only two fixed directions.

The paper introduces a novel approach for two-dimensional in-orbit satellite antenna pattern measurement. A small measurement satellite flies in Double-Cross-Helix formation with the radar satellite. The orbit parameters of the measurement satellite are configured in a way that - with respect to the spherical antenna coordinate system of the radar satellite - it flies through all polar angles at a selectable constant azimuthal angle. This provides a central cut, and numerous central cuts combine to a two-dimensional pattern. All the measurements are performed in free space, which avoids the distortions arising when using on-ground calibration targets. These distortions are caused by atmosphere, ionosphere, ground clutter and multipath effects, ambiguities, and volume scattering. The paper provides a feasible high-level system concept for in-orbit measuring the two-dimensional pattern of a TerraSAR-X like radar satellite, e.g. [1]-[2], with a passive measurement satellite that carries a reflecting sphere as radar reflector.

The literature reports about in-orbit antenna pattern measurement for Medium (MEO) and Geostationary Earth Orbiting (GEO) satellites. The in-orbit Tx pattern measurement of a GPS satellite in 20000 km altitude by means of 8 LEO measurement satellites is discussed in [5] and [6]. Visibilities of the GPS satellite from the LEO measurement satellites are taken as opportunities to obtain cuts through the two-dimensional GPS antenna pattern. After about 3 weeks of measurement with 8 satellites, sufficient cuts are obtained for a two-dimensional Tx azimuth/elevation pattern at a polar angle range constrained to $\pm 13.8°$. Also [7] describes a concept for MEO SAR Tx elevation pattern measurement. It measures the high-gain part of the main lobe by a LEO calibration satellite that is on receive when it crosses this part of the main lobe.

Within 1 year 15 measurement opportunities can be found, and one of them is close to the elevation pattern, i.e. the azimuth angle deviation from the central cut is 0.007°. Concepts for swarms of radar calibration satellites that measure GEO and MEO SAR are provided in [8].

The Double-Cross-Helix measurement as it is derived in this paper is applicable to radar satellites in polar LEO orbits. However, the adaption also to different LEO as well as MEO and GEO orbits appears possible by adapting the derivation to different radar satellite orbits.

The novel approach can contribute to future satellite missions by providing faster, cheaper, more accurate and frequent in-orbit antenna pattern measurements, especially in case of a huge number of electronically steered antenna beams and/or digital beamforming.

For the derivations in the paper, the antenna centers of radar and measurement satellite are assumed to be at their centers of gravity. A right looking acquisition geometry is considered. However, the approach and the formulas provided are valid for left looking as well. It is presumed that the radar satellite is capable to steer its attitude in yaw, pitch and roll angles.

Besides radar satellites, the proposed two-dimensional in-orbit satellite antenna pattern measurement is also of interest for other remote sensing satellites, navigation and communication satellites, too. For the ease of reading, the satellite with the antenna to be measured is denoted as *radar satellite* in the following, which is nonetheless abbreviated as RSS (Radio Signal Satellite) to address the wider spectrum of satellite types that potentially benefit from the novel approach. The small satellite that shapes the Double-Cross-Helix orbit formation and carries a radio reflector or a measurement antenna is referred to as *measurement satellite* (MES).

The paper is organized as follows. In Section II, a feasible high-level system concept is provided that is dedicated to a radar satellite similar to TerraSAR-X. Section III introduces the Double-Cross-Helix concept, and Section IV derives the Double-Cross-Helix orbit parameters for desired central cuts at constant azimuthal measurement angles. Section V provides the measurement satellite orbits calculated for the measurement system. Section VI introduces an alternative calculation approach for the measurement orbits that is based on the difference in the radar and measurement satellite's ascending node drift rates. Section VII provides a first estimation of measurement accuracy and measurement angle sampling distance based on the beforehand calculated Double-Cross-Helix.

II. HIGH-LEVEL SYSTEM CONCEPT OF IN-ORBIT ANTENNA PATTERN MEASUREMENT

This Section provides a high-level description of a feasible measurement system for a SAR satellite similar to TerraSAR-X. The focus is on distance, power and Signal-to-Noise Ratio (SNR). The system concept is complemented in Section VII by accuracy and sampling analyses that consider the Double-Cross-Helix orbits calculated in the succeeding sections. A two-way pattern measurement is considered as is shown in Fig. 1.
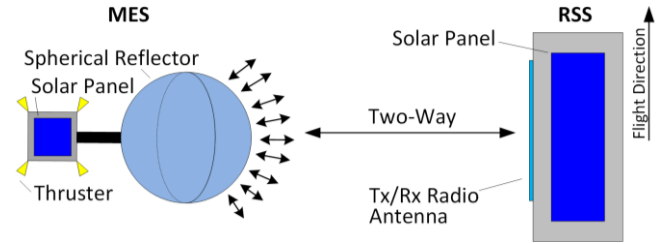

Fig. 1. Two-way pattern measurement. Measurement satellite (MES) with reflecting sphere facing the radio antenna of the radar satellite (RSS).

The measurement satellite MES carries a reflecting sphere that faces the radar satellite's antenna. A reflecting sphere is advantageous in several ways. It has a small radar cross section σ that allows for short measurement distances in terms of power, a direction-independent reflection, and it shields the MES bus structure from the radar illumination. For a constant radar reflection, i.e., a constant σ, and to permanently shield the MES bus structure, the MES attitude should orient the sphere towards the RSS antenna during the entire orbits. In other words, there should always be a virtual straight line between MES satellite bus, reflecting sphere and RSS antenna.

The radar satellite transmits radar pulses, which are reflected from the measurement satellite and then received again from the radar satellite. A chirp waveform, e.g. [19], [22], is selected as measurement signal since it provides an inherent frequency scan of the antenna pattern. It also allows for a range compression to improve the SNR of the measurement signal at larger distances. Fig. 2 (a) illustrates several measurement chirps. The blue window is a partial chirp that is to be compressed. The window moves along the chirp and by this, the center frequency of the partially compressed chirp moves as well. Such a partial moving range compression maintains the frequency dependence of the antenna pattern measurement.

A further option to improve the SNR is to transmit a small number of measurement pulses with a high Pulse Repetition Frequency (*PRF*) at one pseudo-static measurement position, i.e., the measurement angle variation is small versus the measurement angle sample interval (cf. Section VII.C), and to compress the reflected pulse echoes in azimuth. Fig. 2 (b) provides an example number of azimuth compressed (AC) pulses that increase with distance, and is based on the TABLE I and TABLE II parameters. A minimum SNR of 35 dB is maintained by transmitting more than 1 pulse for distances above 8 km.

The power design of the system concept is discussed with respect to a TerraSAR-X like illumination of a 3 m corner reflector with the parameters in TABLE I. The video power P_{video} at the radar antenna output is calculated using

$$P_{video} = \frac{P_{Pk} \cdot \lambda^2 \cdot G_{Tx} \cdot G_{Rx} \cdot \sigma}{(4\pi)^3 \cdot d^4 \cdot L_{Atm}} \qquad (1)$$

with P_{Pk} being the radar peak power, the wavelength λ, the maximum Tx and Rx antenna gains G_{Tx} and G_{Rx}, respectively, the radar cross section σ of the corner reflector, the distance d between radar and on-ground corner reflector, and the two-way atmospheric loss L_{Atm}. The equation is also used for the measurement satellite's reflecting sphere with the corresponding inter-satellite distance, and no atmospheric loss.
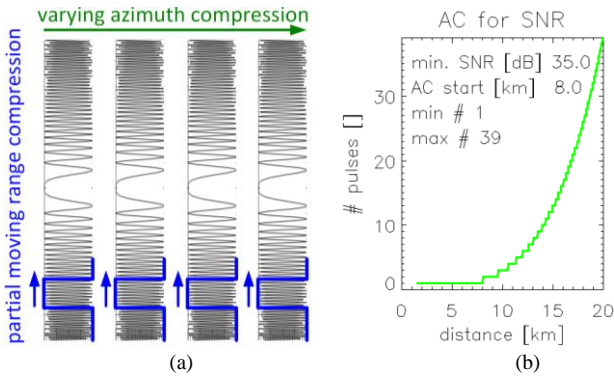
Fig. 2. (a) Partial moving range compression of measurement chirps (blue color) that allows for a frequency-dependent pattern measurement while improving the SNR. Additionally, a small number of pulses are coherently integrated via azimuth compression to further improve the SNR (green color). (b) Number of azimuth pulses to achieve a minimum SNR of 35 dB. The number of required pulses increases with distance.

The resulting P_{video} of -84.6 dBm for the on-ground corner reflector is shown by the red horizontal line in Fig. 3 (a). It is constant due to the fixed slant range distance d of 600 km. After range compression of the full 300 MHz Range Bandwidth Br and the full Pulse Length T_p with the parameters in TABLE I, the corner reflector reference SNR is 35 dB. This value can be found as red horizontal line in Fig. 3 (b). TABLE II provides the parameters that are applied in addition to or instead of TABLE I in the power and noise calculations of the antenna measurement using MES.

TABLE I
TerraSAR-X like parameters for 3 m corner reflector illumination

wavelength λ	0.03106 m	standard temperature	290 K
peak power P_{Pk}	2200 W	system noise figure F_{sys}	4 dB
waveform	chirp	Tx antenna gain G_{Tx}	46.3 dB
range bandwidth B_r	300 MHz	Rx antenna gain G_{Rx}	46.3 dB
PRF	6800 Hz	slant range d	600 km
duty	0.062	corner reflector inner leg	3 m
pulse length T_p	9.1 µs	corner reflector σ	55.5 dBm^2
		two-way atmosph. loss L_{Atm}	2 dB

TABLE II
Measurement satellite's (MES) and radar satellite's (RSS) parameters

MES reflecting sphere illumination		range and azimuth compression	
radius r_r	0.15 m	$B_{r,int}$, $T_{p,int}$	30 MHz, 0.91 µs
σ		minimum SNR	35 dB
	-11.5 dBm^2	azimuth pulses	1 to 39
L_{Atm}	0 dB		

Fig. 3 (a) provides P_{video} for the two-way measurement with the reflecting sphere on-board the measurement satellite as a function of distance d in black color. Within the calculated distance variation from 1.5 km up to 20 km, P_{video} decreases from about 40 dB above to 6 dB below the TSX reference.

The black line in Fig. 3 (b) shows the SNR after partial moving range compression with a $B_{r,int}$ of 30 MHz and a $T_{p,int}$ of 0.91 µs. Again, the horizontal line in red color shows the SNR of a TerraSAR-X like illumination of a 3 m corner reflector after range compression with 300 MHz at a constant distance of 600 km. The dashed green line shows the SNR after additional azimuth compression of the small number of pulse echoes $N_{az,int}(d)$ from Fig. 2 (b), which increases with distance d to keep the SNR above 35 dB, which is the identical value of the on-ground corner reflector, and which provides a gain accuracy better than 0.05 dB (cf. Section VII.A). The small spikes are

due to the integer pulse numbers. The SNR after partial range compression and a distance-dependent number of integrated azimuth pulses is calculated by (2).
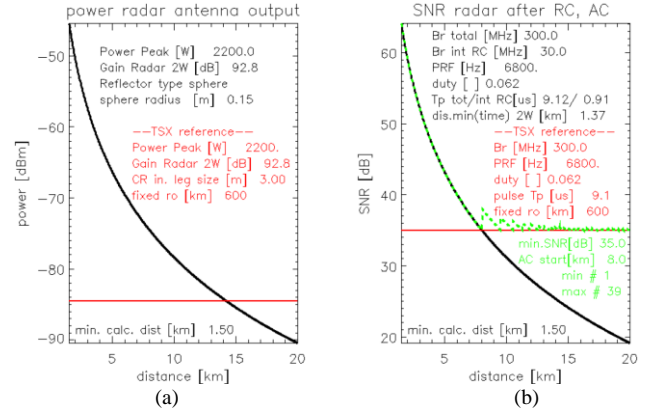

Fig. 3. Power at radar antenna output and SNR in comparison to a 3 m on-ground corner reflector illumination (red horizontal lines). (a) Power at antenna output for two-way measurement. (b) SNR for two-way measurement with partial moving range compression (black) and additional azimuth compression of few pulses (green). TSX reference with full range compression and without azimuth compression (red).

$$SNR = \frac{P_{S,RC,AC}}{P_N} = \frac{P_{video} \cdot B_{r,\text{int}} \cdot T_{p,\text{int}} \cdot N_{az,\text{int}}(d)}{k_0 \cdot T_0 \cdot B_{r,\text{int}} \cdot F_{sys}} \qquad (2)$$

The length of the total chirp T_p in the example is 9.1 µs, which corresponds to a minimum required two-way distance d of 1.37 km considering the echo window timing of a pulsed radar system.

The conclusion of this subsection is that for a TerraSAR-X like example SAR system and a 15 cm radius reflecting sphere, a distance range between 1.5 and 20 km is reasonable in terms of signal power, SNR and echo timing. After deriving the Double-Cross-Helix orbits in the next Sections, the discussion of the high-level system concept continues in Section VII using these orbits.

III. DOUBLE-CROSS-HELIX ORBIT

The Double-Cross-Helix is an extension of the Helix concept known from the TanDEM-X mission [13],[14],[15]. In a Helix-configuration, in one orbit revolution the measurement satellite completely revolves the radar satellite, and thus sweeps through a 360° angular range. This characteristic can be utilized to implement an in-orbit antenna pattern measurement. A TanDEM-X Helix [10],[11],[12] is created by two polar orbits with small differences in the eccentricities Δe and the arguments of the ascending nodes $\Delta\Omega$ in combination with identical arguments of perigee $\omega = 90°$.

The two left drawings of Fig. 4 schematically show the effect of Δe and $\Delta\Omega$. The eccentricity difference Δe causes a radial baseline $B_{rad,\Delta e}$ that is maximum at the poles and zero at the equators. The term baseline (B) is widely used to denote the distance between two antennas. Radial means the projection into the radial direction, and the creator Δe of this baseline component is annotated in the subscript. An along-track baseline component $B_{along,\Delta e}$ is also generated by Δe. It is maximum at the equator and zero at the poles. The difference in the ascending nodes $\Delta\Omega$ causes a cross-track baseline $B_{cross,\Delta\Omega}$ that is maximum at the equator and zero at the poles.
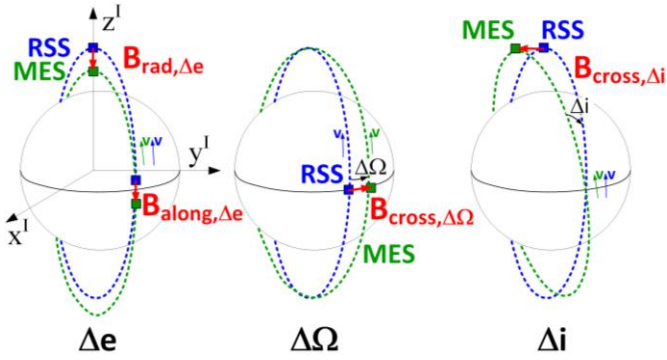
Fig. 4. Illustration of the basic radial, along-track and across-track baseline components that are generated by one different orbit parameter, i.e. either eccentricity, inclination or argument of the ascending node. The argument of perigee ω is 90°.

A TanDEM-X Helix is a safe orbit formation because the radial and the cross-track baseline components are never zero at the same time, which means the two orbits do never cross. Below in this Section, it will be shown that a TanDEM-X Helix can be used to measure the pattern of a nadir looking antenna. To measure also side-looking antennas as for example a SAR antenna, the TanDEM-X Helix is complemented to a Double-Cross-Helix by a second cross-track component that is induced by an inclination difference Δi. The resulting cross-track baseline component $B_{cross,\Delta i}$ is schematically shown in the right drawing of Fig. 4. It is maximum at the poles and minimum at the equator. An inclination difference causes different rotation rates of the ascending nodes and should be considered (cf. Section VI).

The Double-Cross-Helix orbit concept is developed in the succeeding subsections, starting from the radar antenna coordinate system and after introducing several coordinate systems that are required in the derivations.

A. Antenna Coordinate System

Fig. 5 illustrates the antenna pattern of the radar satellite in its Cartesian *Antenna* coordinate system A with the axes x^A, y^A, and z^A. The superscript letter indicates the respective reference system. The Cartesian coordinates can unambiguously be transformed into the spherical coordinates radial distance d, polar angle ψ and azimuthal angle ξ by using

$$\sin\xi = \frac{B_{cross}^A}{\sqrt{\left(B_{along}^A\right)^2 + \left(B_{cross}^A\right)^2}} \; ; \; \xi \in \left[-90°, 90°\right[$$

$$\tan\psi = \frac{\sqrt{\left(B_{along}^A\right)^2 + \left(B_{cross}^A\right)^2}}{B_{rad}^A} ; \; \psi \in \left[-90°, 90°\right] \qquad (3)$$

$$d = \sqrt{\left(B_{along}^A\right)^2 + \left(B_{cross}^A\right)^2 + \left(B_{rad}^A\right)^2}$$

The components of the vector formed between the origin of A and the position of the measurement satellite are the along-track baseline B_{along}^A, the across-track baseline B_{cross}^A, and the radial baseline B_{rad}^A. This vector is the baseline vector. Its length is d and equal to the distance between the radar and the measurement satellite.
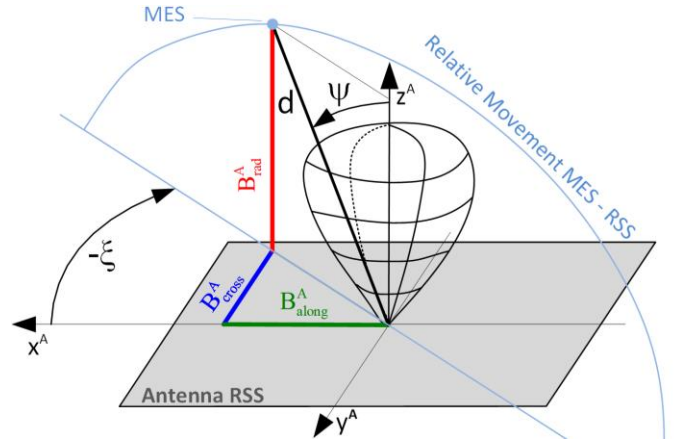

Fig. 5. Cartesian *Antenna* coordinate system A of the radar satellite RSS, and corresponding spherical coordinates radial distance d, polar angle ψ and azimuthal angle ξ. The position of the measurement satellite MES w.r.t. the antenna center is composed of the orthogonal baseline components B_{along}^A, B_{cross}^A, and B_{rad}^A. On its orbit, the MES relative movement shall provide all polar angles ψ at a fixed azimuthal angle ξ.

For the measurement, the antenna pattern is considered to be two-dimensional in polar angle ψ and azimuthal angle ξ whereas the distance d is available from the measurement geometry for each ξ-ψ-combination, i.e., it can be considered to be known to high accuracy. In the following, the measurement satellite orbit parameters are derived in such a way that the relative movement of the measurement satellite along its orbit spans all polar angles ψ at a constant and adjustable azimuthal angle ξ. This is shown in Fig. 5 by the blue bow that symbolizes this relative movement. By changing the orbit parameters of the measurement satellite, different central cuts through the two-dimensional pattern can be obtained.

B. Satellite Coordinate Systems

For the derivation of the Double-Cross-Helix orbit the following radar satellite coordinate systems need to be considered. Apart from the *Inertial* system, all systems have their origin at the radar satellites antenna center. The approximation of identical satellite center of mass and antenna center is made.

- The *Inertial* system I is an Earth-centered inertial frame. The Earth's equatorial plane is the fundamental x^I-y^I-plane where the x^I-axis points in the vernal equinox direction. The z^I-axis is along the direction of the North Pole [17]. This system does not rotate, and the satellites' position and velocity vectors are estimated in this system.
- The *Local* system L is a rotating frame that is different for each orbit position and is built from the radial direction vector and the anti-angular-momentum direction vector, both in *Inertial* system coordinates.
- The *Body* system B is rigidly coupled to the radar satellite's body and is obtained from the *Local* system through rotations by the attitude angles.
- The *Antenna* system A (cf. also Fig. 5) is oriented into the side-looking direction of the acquisition. It arises from the *Body* system by rotation with the side-looking offset angle θ_{off} that spans between nadir direction and main antenna illumination direction.

- The *rotated Antenna* system Ar is rotated around the antenna's z^A-axis w.r.t. the *Antenna* system by the azimuthal offset angle ξ_{off}. It is interposed between the *Body* and *Antenna* systems in order to optimize the azimuthal angle of the antenna pattern measurement. The *rotated Antenna* system is applied below in Section IV.B.

The *Local* system is defined by the orthogonal vectors in equation (4) with $\mathbf{r}^I_{RSS}$ and $\mathbf{v}^I_{RSS}$ being the radar satellite's *Inertial* system position and velocity vectors.

$$\hat{\mathbf{z}}^L = -\frac{\mathbf{r}^I_{RSS}}{r^I_{RSS}} \; ; \; \hat{\mathbf{y}}^L = -\frac{\mathbf{r}^I_{RSS} \times \mathbf{v}^I_{RSS}}{r^I_{RSS} \cdot v^I_{RSS}} \; ; \; \hat{\mathbf{x}}^L = \hat{\mathbf{y}}^L \times \hat{\mathbf{z}}^L$$

$$\mathbf{B}^L = \left[\hat{\mathbf{x}}^L \; \hat{\mathbf{y}}^L \; \hat{\mathbf{z}}^L\right]^T \cdot \left(\mathbf{r}^I_{MES} - \mathbf{r}^I_{RSS}\right) = {}^L D^I \cdot \left(\mathbf{r}^I_{MES} - \mathbf{r}^I_{RSS}\right) = \begin{bmatrix} B^L_{along} \\ B^L_{cross} \\ B^L_{rad} \end{bmatrix} \quad (4)$$

The circumflex indicates unity vectors and r^I_{RSS} and v^I_{RSS} are position and velocity absolute values, respectively. Transforming the difference of the measurement and radar satellites' position vectors from the *Inertial* into the *Local* system provides the baseline vector $\mathbf{B}^L$ in the *Local* system. In (4), ${}^L D^I$ is a rotation matrix that transforms a vector from the *Inertial* into the *Local* system. Next, the radar satellite's attitude steering angles yaw α, pitch β, and roll γ in (5) rotate the baseline vector from the *Local* into the *Body* system.

$$\mathbf{B}^B = \begin{bmatrix} 1 & 0 & 0 \\ 0 & \cos\gamma & \sin\gamma \\ 0 & -\sin\gamma & \cos\gamma \end{bmatrix} \cdot \begin{bmatrix} \cos\beta & 0 & -\sin\beta \\ 0 & 1 & 0 \\ \sin\beta & 0 & \cos\beta \end{bmatrix} \cdot \begin{bmatrix} \cos\alpha & \sin\alpha & 0 \\ -\sin\alpha & \cos\alpha & 0 \\ 0 & 0 & 1 \end{bmatrix} = {}^B D^L \cdot \mathbf{B}^L \quad (5)$$

For the further derivation, we assume that the initial radar satellite's attitude steering angles α, β, and γ are zero, and thus $\mathbf{B}^B$ equals $\mathbf{B}^L$. The next system is the *rotated Antenna* system that is an intermediate system towards the *Antenna* system. The side-looking offset angle θ_{off} transforms the baseline vector from the *Body* into the *rotated Antenna* system. θ_{off} is a rotation about the x^B-axis of the *Body* system and describes the offset rotation of the z^{Ar} axis away from the nadir direction. For $|\theta_{off}| \leq 90°$, a positive side-looking offset angle θ_{off} results in a so-called right looking system.

$$\mathbf{B}^{Ar} = \begin{bmatrix} 1 & 0 & 0 \\ 0 & \cos\theta_{off} & -\sin\theta_{off} \\ 0 & +\sin\theta_{off} & \cos\theta_{off} \end{bmatrix} \cdot \mathbf{B}^B = {}^{Ar} D^B \cdot \mathbf{B}^B \quad (6)$$

The *rotated Antenna* system allows the use of azimuthal offset angles ξ_{off} that optimize the azimuthal angle of the antenna pattern measurement. ξ_{off} is a rotation around the z^{Ar}-axis and is discussed in detail in Section IV.B.

$$\begin{bmatrix} B^A_{along} \\ B^A_{cross} \\ B^A_{rad} \end{bmatrix} = \mathbf{B}^A = \begin{bmatrix} \cos\xi_{off} & +\sin\xi_{off} & 0 \\ -\sin\xi_{off} & \cos\xi_{off} & 0 \\ 0 & 0 & 1 \end{bmatrix} \cdot \mathbf{B}^{Ar} = {}^A D^{Ar} \cdot \mathbf{B}^{Ar} \quad (7)$$

Finally, from the components B^A_{along}, B^A_{cross}, and B^A_{rad} of the baseline vector, the polar angle ψ and the azimuthal angle ξ can be calculated using (3).

C. Standard-Helix Orbit

The kind of Helix-orbit flown by the TanDEM-X mission [10], [13] is a good starting point for the derivation of a suitable orbit that allows for the measurement of antenna pattern central cuts. It is denoted by *Standard-Helix* in the following. The reason is that during an orbit one satellite revolves the other completely in all three dimensions of the *Local* coordinate system of the revolved satellite. For a Standard-Helix, the along-track baseline $B^L_{along,\Delta e}$ and the radial baseline $B^L_{rad,\Delta e}$ of Fig. 4 can be approximately described by

$$B^L_{rad,\Delta e}(u) \approx B^L_{rad,\Delta e,max} \cdot \sin u \approx a \cdot \Delta e \cdot \sin u$$
$$B^L_{along,\Delta e}(u) \approx B^L_{along,\Delta e,max} \cdot \cos u \approx -2 \cdot a \cdot \Delta e \cdot \cos u \quad (8)$$

with the perigees ω of the measurement and the radar satellites both being at the argument of latitude $u = 90°$, the semi-major axis being denoted as a and the difference of the eccentricities [16] being denoted as $\Delta e = e_{MES} - e_{RSS}$. The maxima of the radial baseline $B^L_{rad,\Delta e,max}$ are at an argument of latitude $u = \pm 90°$, and the ones of the along-track baseline $B^L_{along,\Delta e,max}$ are at equator.

The cross track-baseline $B^L_{cross, \Delta\Omega}$ of the Standard-Helix is induced by a difference in the right ascension of the ascending nodes $\Delta\Omega = \Omega_{MES} - \Omega_{RSS}$ [10], [13]. As is shown by Fig. 4, the maxima of this cross-track baseline $B^L_{cross,\Delta\Omega,max}$ are at the equator, and a value of zero results for an argument of latitude $u = \pm 90°$.

$$B^L_{cross,\Delta\Omega,max} \approx \sin i_{RSS} \cdot a \cdot (1 - e^2_{RSS}) \cdot \sin \Delta\Omega$$
$$B^L_{cross,\Delta\Omega}(u) \approx B^L_{cross,\Delta\Omega,max} \cdot \cos u \approx \sin i_{RSS} \cdot a \cdot (1 - e^2_{RSS}) \cdot \sin \Delta\Omega \cdot \cos u \quad (9)$$

From Fig. 5, it can be concluded that a Central Orbit Position (COP) is required w.r.t. the *Antenna* system, where both the cross-track and the along-track baseline components are zero, i.e. $B^A_{cross} = B^A_{along} = 0$, and the radial baseline component B^A_{rad} is positive and significantly greater than zero. If this condition is fulfilled, then the one-dimensional central cuts for all different azimuthal angles intersect at this central orbit position COP.

For the Standard-Helix and by setting - in addition to the zero attitude angles - also the angles θ_{off} and ξ_{off} to zero, i.e. $\mathbf{B}^A = \mathbf{B}^L$, the central orbit position is located at the perigee $u = 90°$. This is illustrated in Fig. 6 (a).

Since the cross-track baseline B^A_{cross} of the Standard-Helix is generated by a difference in the ascending nodes $\Delta\Omega$, it is zero at $u = 90°$. Thus, at $u = 90°$ also the along-track baseline B^A_{along} needs to be zero, and therefore, the perigees of radar and measurement satellites are set to be at $u = 90°$. Since a Standard-Helix has the just described baseline configuration of Fig. 6 (a), the main radar antenna illumination at $u = 90°$ is into the direction of the z^L-axis, which is with $\alpha = \beta = \gamma = \theta_{off} = \xi_{off} = 0°$ identical to the z^A-axis. The z^L-axis directs toward nadir and thus, a nadir looking antenna can principally be measured with an additional measurement satellite flying in a Standard-Helix.
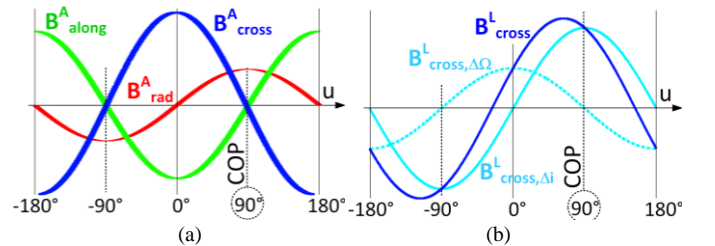

Fig. 6. (a) Baseline components for a Standard-Helix with $\alpha = \beta = \gamma = \theta_{off} = \xi_{off} = 0°$ in the radar satellite's *Antenna* system. $\mathbf{B}^A = \mathbf{B}^L$. (b) The two cross-track baselines of the Double-Cross-Helix in the radar satellite's *Local* system (light-blue color) and the sum of the two (dark-blue color).

D. Cross-Track Baseline Component Rising from Δi

In the more general case of a side-looking system like SAR, the side-looking offset angle θ_{off} is different from zero, and the Standard-Helix cannot be used since the baseline vector in the *Local* and in the *Antenna* coordinate systems are different, i.e., $\mathbf{B^L} \neq \mathbf{B^A}$. For the right looking acquisition geometry of the high-level system concept considered in this paper, the side-looking offset angle θ_{off} is 33.8°. This corresponds to the value used in TerraSAR-X.

Fig. 7 illustrates how a generic side-looking offset angle θ_{off} of a side-looking geometry can be accounted for by using an inclination difference $\Delta i = i_{MES} - i_{RSS}$ between the measurement and radar satellites' orbits. The inclination difference generates a second cross-track baseline component, which positions the measurement satellite into the radar satellite's main illumination direction.
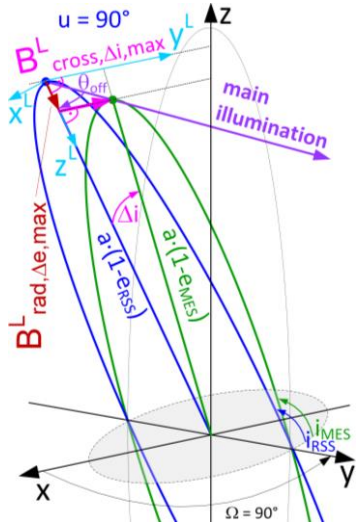

Fig. 7. Radar satellite's orbit in blue color and measurement satellite's orbit in green color for $\Delta e > 0$, $\Delta i < 0°$ and $\Delta\Omega = 0°$. The measurement satellite is positioned into the main illumination direction of the radar antenna at $u = 90°$ for a right-looking system with a positive side-looking offset angle θ_{off}. For illustration, Ω is set to 90°. The assumption is made that the attitude steering angles $\alpha = \beta = \gamma = 0°$, and thus $\mathbf{B^B} = \mathbf{B^L}$.

An inclination difference generates maxima of the cross-track baseline $B^L_{cross,\Delta i,max}$ in the *Local* system at $u = \pm 90°$ and its minima at the equator. $B^L_{cross,\Delta i,max}$ can be derived from Fig. 7 and is given in (10). The cross-track baseline $B^L_{cross,\Delta i}(u)$ that is induced by an inclination difference Δi can be approximated by a sinusoidal function.

$$\mathrm{B}^L_{cross,\Delta i}\left(u\right) \approx \mathrm{B}^L_{cross,\Delta i,max} \cdot \sin u \approx a \cdot \left(1 \mp \left(e_{RSS} + \Delta e\right)\right) \cdot \sin\Delta i \cdot \sin u \quad (10)$$

The minus of the $\mp$ sign is for a measurement around the central orbit position COP at perigee, the plus is for apogee. This is discussed in detail in Appendix A.

For a positive eccentricity difference Δe, i.e. $e_{MES} > e_{RSS}$, the maximum of the radial baseline $B^L_{rad,\Delta e,max}$ is positive at $u = 90°$ as is shown in Fig. 7. Following the discussion before, the maximum of the cross-track baseline $B^L_{cross,\Delta i,max}$ must also be positive in order to position the measurement satellite into the main illumination direction of the radar satellite, which points obliquely downward toward the Earth's surface. As it can be seen in Fig. 7, the ratio of these cross-track and radial baseline components is equal to the tangent of the side-looking offset angle θ_{off}.

$$\tan\theta_{off} \approx \frac{\mathrm{B}^L_{cross,\Delta i,max}}{\mathrm{B}^L_{rad,\Delta e,max}} \quad (11)$$

A detailed discussion on the radial and cross-track baseline components and the positioning of the measurement satellite into the main illumination direction of the radar antenna is provided in Appendix A. Here, the approximation is made that the attitude steering angles $\alpha \approx \beta \approx \gamma \approx 0°$, and thus $\mathbf{B^B} = \mathbf{B^L}$. In case α, β, and γ deviate considerably from zero, the components of the baseline vector $\mathbf{B^B}$ in the *Body* system should be used in (11). Otherwise, the components of the *Local* system baseline vector $\mathbf{B^L}$ the can be used. This is more convenient for the derivations and was also done so in Sections III and IV.

E. Double-Cross-Helix Geometry

A Helix built only by means of an inclination difference Δi and an eccentricity difference Δe is not safe since at the equator both the radial and the cross-track baseline components $B^L_{rad,\Delta e}$ and $B^L_{cross,\Delta i}$ are zero, which means the orbits are crossing. Fig. 6 (b) shows an example $B^L_{cross,\Delta i}(u)$ in light blue color continuous line style.

In order to obtain a safe Helix-configuration, a further cross-track baseline contribution induced by a difference in the ascending nodes $\Delta\Omega$ is required, since this cross-track baseline contribution is maximum at the equator where the radial baseline component is zero (cf. [10]). Fig. 6 (b) shows an example cross-track baseline $B^L_{cross,\Delta\Omega}$ that is induced in this way by a $\Delta\Omega$ in light blue dotted line style. The sum of the cross-track baselines B^L_{cross} that results from the Δi and $\Delta\Omega$ induced contributions is plotted in dark blue color. In case equation (11) is fulfilled, the transformation of the baseline vector $\mathbf{B^L}$ from the *Local* into the *Antenna* system $\mathbf{B^A}$ by means of the side-looking offset angle θ_{off} (with $\alpha = \beta = \gamma = \xi_{off} = 0°$) results in a total cross-track baseline component B^A_{cross} in the manner of Fig. 6 (a) that is zero at $u = 90°$, and has its maximum at the equator.

The geometry of a Double-Cross-Helix is provided in Fig. 8. From this geometry and the lower enlarged area, the maximum of the cross-track baseline component $B^L_{cross,\Delta\Omega,max}$ that is induced by $\Delta\Omega$ can be derived to the first line of (12). The second line is an approximation for a small Δi that is identical to the first line in (9).

$$\mathrm{B}^L_{cross,\Delta\Omega,max} = \frac{\sin i_{MES} \cdot a \cdot \left(1 - e^2_{RSS}\right) \cdot \sin\Delta\Omega}{\cos\left(i_{MES} - i_{RSS}\right)}$$

$$\mathrm{B}^L_{cross,\Delta\Omega,max}\Big|_{i_{MES} \approx i_{RSS}} \approx \sin i_{RSS} \cdot a \cdot \left(1 - e^2_{RSS}\right) \cdot \sin\Delta\Omega \quad (12)$$

Because of the two cross-track contributions, at perigee position $u = 90°$, an additional small baseline $\mathbf{\Delta B^L}$ arises whose radial and cross-track components can be neglected for the derivations in this paper. Its along-track component ΔB^L_{along} is required below in Section IV.D, and it can be derived from Fig. 8 and the upper enlarged area to the expression in (13).

$$\Delta\mathrm{B}^L_{along} \approx -a \cdot \left(1 \mp \left(e_{RSS} + \Delta e\right)\right) \cdot \sin\left(i_{MES} - 90°\right) \cdot \sin\Delta\Omega \quad (13)$$

For the $\mp$ sign please refer to Appendix A.
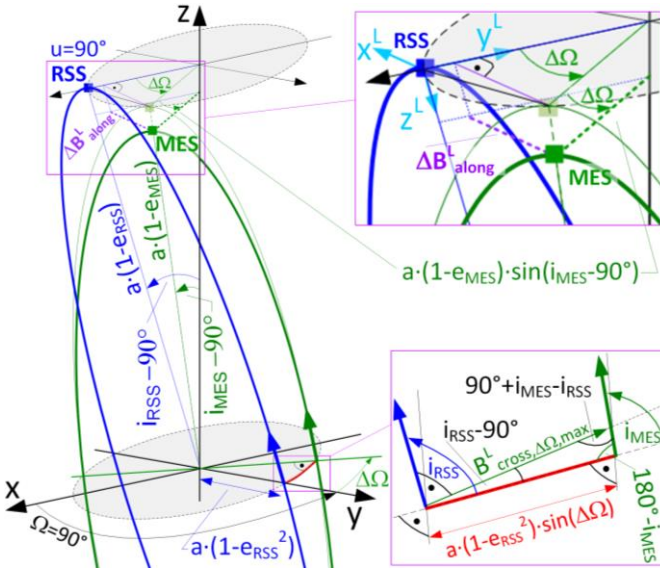
Fig. 8. Double-Cross-Helix geometry with cross-track baseline contributions from an inclination difference $\Delta i < 0°$ and an eccentricity difference $\Delta e > 0$. The difference in the ascending nodes $\Delta\Omega$ is positive. From this geometry the maximum cross-track baseline $B^L_{cross,\Delta\Omega,max}$ due to $\Delta\Omega$ and the along-track component of the additional small baseline ΔB^L_{along} can be derived. For illustration Ω is set to $90°$.

IV. DOUBLE-CROSS-HELIX ORBIT PARAMETERS

The derivation of the Double-Cross-Helix parameters is supported by plots that are generated from the orbit parameters in TABLE III that are similar to the ones of TerraSAR-X. The measurement satellite's orbit parameters result from the derived differences between the orbit parameters of the radar and measurement satellite. The semi-major axis a and the argument of perigee ω are identical for both satellite orbits.

TABLE III
Example Orbit Parameters

	RSS		MES	
semi-major axis	a_{RSS}	6892 km	a_{MES}	$= a_{RSS}$
argument of perigee	ω_{RSS}	90°	ω_{MES}	$= \omega_{RSS}$
eccentricity	e_{RSS}	0.0011	e_{MES}	$= e_{RSS} + \Delta e$
inclination	i_{RSS}	97.455°	i_{MES}	$= i_{RSS} + \Delta i$
right ascension of the ascending node	Ω_{RSS}	90°	Ω_{MES}	$= \Omega_{RSS} + \Delta\Omega$
orbit time at COP	τ_{RSS}	0 s	τ_{MESS}	$= \tau_{RSS} + \Delta\tau$
side-looking offset angle (right looking)	θ_{off}	33.8°		

A. Pattern Measurement at a Constant Azimuthal Angle ξ

This Section derives the eccentricity difference Δe and the inclination difference Δi that are required to obtain a central cut through the two-dimensional antenna pattern at a desired fixed azimuthal angle ξ, while the relative motion of the measurement satellite around the radar satellite results in a continuous variation of the polar angle ψ (cf. Fig. 5). The difference in the ascending nodes $\Delta\Omega$ is an input to the derivation. In Section IV.C, it is explained how $\Delta\Omega$ has to be set by considering the desired measurement distances and the orbit altitude of the measurement satellite.

From the first line of (3) and (6), and with $\alpha \approx \beta \approx \gamma \approx \xi_{off} \approx 0°$, the angle ξ can be written as a function of the components of the baseline vector $\mathbf{B^L}$ in the *Local* system. Equation (14) results from using the sum of the $\Delta\Omega$ and Δi contributions to the total cross-track baseline $B^L_{cross}(u)$, which are defined in (9) and (10). The along-track and radial components are defined in (8).

$$\tan\xi = \frac{\left[B^L_{cross,\Delta\Omega}(u) + B^L_{cross,\Delta i}(u)\right]\cdot\cos\theta_{off} - \sin\theta_{off}\cdot B^L_{rad,\Delta e}(u)}{B^L_{along,\Delta e}(u)} \tag{14}$$

Equation (11) is valid for an argument of latitude $u = 90°$. In approximation, it is also used for the surrounding, and the side-looking offset angle θ_{off} is approximated by (15).

$$\tan\theta_{off} \approx \frac{B^L_{cross,\Delta i}(u)}{B^L_{rad,\Delta e}(u)} \tag{15}$$

Substituting $B^L_{cross,\Delta i}(u)$ in (14) with (15) eliminates $B^L_{rad}(u)$, and after insertion of (9) and (10), the equation can be resolved for the eccentricity difference Δe.

$$\Delta e \approx -\frac{\sin i_{RSS}\cdot\left(1 - e^2_{RSS}\right)\cdot\sin\Delta\Omega\cdot\cos\theta_{off}}{2\cdot\tan\xi} \tag{16}$$

This equation calculates for a desired azimuthal angle ξ the eccentricity difference Δe that places the measurement satellite at $u = 90°$ into the main illumination direction θ_{off} of the radar satellite. The associated inclination difference Δi is obtained from (15) by inserting the expressions for $B^L_{rad}(u)$ and $B^L_{cross,\Delta i}(u)$ from (8) and (10), respectively.

$$\Delta i \approx (-1)\cdot\text{asin}\left(\frac{\tan\theta_{off}\cdot\Delta e}{1 \mp (e_{RSS} + \Delta e)}\right) \tag{17}$$

Appendix A explains the term (-1), the $\mp$ sign, and whether it is necessary to measure around the central orbit position COP at perigee or apogee.

B. Azimuthal Offset Angle ξ_{off}

Considering (16), the difference in the eccentricities Δe becomes too large for azimuthal angles ξ close to $0°$ because that would mean a too elliptical orbit of the measurement satellite with too large altitude variation. On the other hand, azimuthal angles close to $\pm90°$ result in a too small eccentricity difference Δe, that would mean almost identical and thus unsafe radar and measurement satellite orbits in terms of radial and along-track baselines. For the orbit parameters in TABLE III, Fig. 9 (a) provides Δe as a function of the azimuthal angle ξ for different values of $\Delta\Omega$ in different colors.

Small rotations of the radar satellite around its antenna z-axis z^A by an azimuthal offset angle ξ_{off} are therefore introduced to keep the measurement satellite's orbit close to circular and distinct enough from that of the radar satellite. Rotations by an azimuthal offset angle ξ_{off} have already been introduced by equation (7).

The azimuthal angle ξ is split-off into an azimuthal cut angle ξ_{cut} and an azimuthal offset angle ξ_{off}. As is indicated in (18) by the superscripts, the azimuthal angle ξ refers to the *Antenna* system A, while the azimuthal cut angle ξ_{cut} refers to the *rotated Antenna* system Ar.

$$\xi^A = \xi^{Ar}_{cut} + \xi_{off} \Rightarrow \xi = \xi_{cut} + \xi_{off} \Leftrightarrow \xi_{cut} = \xi - \xi_{off} \qquad (18)$$

Please note that these superscripts are often omitted in the following to allow for a better reading flow. Fig. 9 (b) shows an example of ξ_{off} values that keep a margin of 25° for $|\xi|$ away from the extreme values 0° and ±90°.
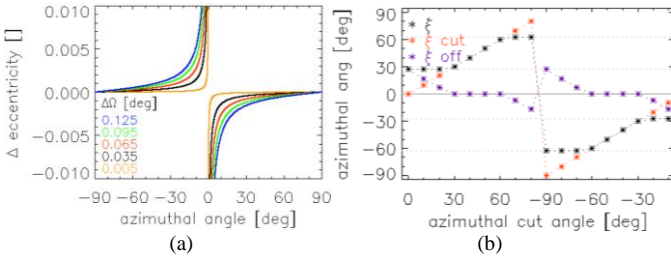

Fig. 9. (a) Eccentricity difference Δe as a function of the azimuthal angle ξ for various differences in the ascending nodes $\Delta\Omega$ in distinct colors. (b) Example for a minimum required azimuthal angle ξ margin of 25° at 0° and ±90°.

Fig. 10 illustrates the rotation by the azimuthal offset angle ξ_{off} around the z^A-axis. The top drawing shows a relative measurement orbit that follows a pattern cut at a negative desired azimuthal cut angle $-\xi_{cut}$, which is for $\xi_{off} = 0°$ identical to $-\xi$ (cf. Fig. 5).

A small example might be helpful. Suppose the desired azimuthal cut angle ξ^{Ar}_{cut} is -80°, and for an offset angle ξ_{off} of zero the azimuthal angle ξ^A is -80°, too. Suppose further that the -80° are too close to -90° since it causes a too small difference in the eccentricities Δe (cf. Fig. 9 (a)), and that the limit for the azimuthal angle ξ^A is set to -65° due to a 25°-margin. Thus, the antenna is rotated around its z^A-axis by and offset angle ξ_{off} of 15° into the *rotated Antenna* System Ar that is shown in the bottom drawing of Fig. 10. In this system, the azimuthal angle ξ^A is reduced to the allowed -65°, but the desired azimuthal cut angle ξ^{Ar}_{cut} is obtained with the means of the additional ξ_{off}-rotation. The measurement orbit parameters are calculated from the azimuthal angle ξ^A of -65° (c.f. Fig. 9 (b)).

Appendix B shows that the mechanical rotation of the radar satellite by the azimuthal offset angle ξ_{off} can be realized by updating the yaw α, pitch β and roll γ angles of the radar satellite into the values $\hat{\alpha}$, $\hat{\beta}$, and $\hat{\gamma}$.

C. Trade-Off for Delta Ascending Node $\Delta\Omega$

A suitable value for the difference in the ascending nodes $\Delta\Omega$ is found by trading-off with the maximum difference in orbit altitude Δh_{max}, and the minimum and maximum length of the baseline vector, d_{min} and d_{max}, respectively. In Section II, d is the distance of the reflecting sphere on-board the measurement satellite to the radar satellite's antenna. The approximated equations in (19) are derived in Appendix C.

$$d_{min} \approx 0.5 \cdot a \cdot \sin i_{RSS} \cdot \sin\Delta\Omega \cdot \tan\left(\max\left[\xi_{off,+90°}, \xi_{off,-90°}\right]\right)$$

$$d_{max} \approx a \cdot \sin i_{RSS} \cdot \sin\Delta\Omega \cdot \sqrt{\left(\frac{\cos\theta_{off}}{\tan\xi_{off,0°}}\right)^2 + 1} \qquad (19)$$

$$\Delta h_{max} \approx 0.5 \cdot a \cdot \sin i_{RSS} \cdot \sin\Delta\Omega \cdot \cos\theta_{off} \cdot \frac{1}{\tan\left(\left|\xi_{off,0°}\right|\right)}$$
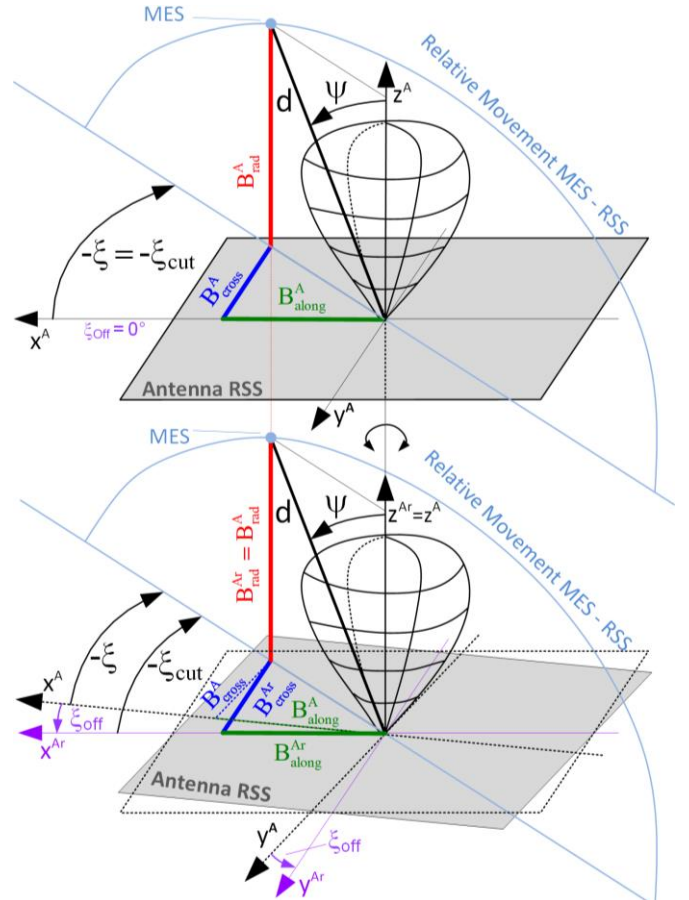

Fig. 10. (top) Orbit of the measurement satellite in the radar satellite's *Antenna* system that provides a desired azimuthal angle $-\xi$ that is equal to an azimuthal cut angle $-\xi_{cut}$ for an azimuthal offset angle $\xi_{off} = 0°$. (bottom) After a rotation around the z^A-axis by the azimuthal offset angle ξ_{off} into the *rotated Antenna* System Ar, ξ is divided into an azimuthal cut angle ξ_{cut} and an azimuthal offset angle ξ_{off}. The measurement orbit's parameters are derived from the azimuthal angle ξ.

with $\xi_{off,+90°}$, $\xi_{off,-90°}$ and $\xi_{off,0°}$ being the distinct azimuthal offset angles assigned to the azimuthal cut angles ξ_{cut} of 90°, -90° and 0°, respectively. For several values of $\xi_{off,-90°}$ and $\xi_{off,0°}$, and the parameters of the high-level system concept, Fig. 11 provides in distinct colors the resulting minimum and maximum distances d_{min} and d_{max}, respectively, and the maximum difference in the satellite's orbit altitude Δh_{max} as a function of the difference in the ascending nodes $\Delta\Omega$. The top plot provides d_{min} for several values of the distinct azimuthal offset angle $\xi_{off,-90°}$. In the bottom plot, the maximum distance d_{max} and the maximum difference in orbit altitude Δh_{max} are plotted for several values of the distinct azimuthal offset angle $\xi_{off,0°}$. Note that in accordance to Fig. 9 (b), only $\xi_{off,-90°}$ is considered here.

The trade-off should also consider that the difference in the ascending nodes $\Delta\Omega$ should be rather small in order to keep the required ΔV for the adjustment of different measurement orbits low. The power at the radar antenna output as well as the two-way time delay are also to be considered (cf. Section II). Finally, the absolute values of the distinct azimuthal offset angles $\xi_{off,\pm90°}$ and $\xi_{off,0°}$ should be moderate in order not to rotate the radar satellite too much out of its nominal position, i.e. moderate updates of the attitude angles α, β, and γ.
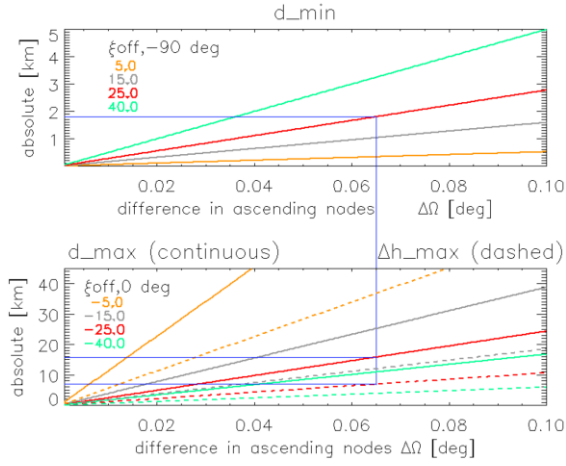
Fig. 11. Trade-off parameters minimum and maximum measurement distance d_{min}, d_{max} and maximum difference in orbit altitude Δh_{max} for the high-level system concept for several values of the distinct azimuthal offset angles $\xi_{off,-90°}$ and $\xi_{off,0°}$ as a function of the difference in the ascending nodes $\Delta\Omega$. The blue horizontal and vertical lines indicate the parameter values that correspond to the selected trade-off value of 0.065° for $\Delta\Omega$.

Using the parameters of the high-level system concept, we start the trade-off by setting the minimum distance d_{min} to 1.8 km. This is sufficient in terms of orbit formation safety, w.r.t. the two-way time delay, and in terms of signal power and SNR (cf. Fig. 3). A value of 25° is selected for the distinct azimuthal offset angle $\xi_{off,-90°}$, and the difference in the ascending nodes $\Delta\Omega$ is traded from (19) and Fig. 11 to a value of 0.065°. Selecting the distinct azimuthal offset angle $\xi_{off,0°}$ to -25° results in a maximum distance d_{max} of 15.8 km and a maximum difference in orbit altitude Δh_{max} of 6.9 km.

According to (16), for *positive* azimuthal angles, the eccentricity difference Δe is negative. This adds an additional constraint to the trade-off for the azimuthal offset angle ξ_{off}, i.e. the eccentricity of the measurement satellite e_{MES} must not be negative. This means the eccentricity difference Δe cannot be larger than the eccentricity of the radar satellite e_{RSS}.

D. Final Adjustments and Derivation Summary

One effect of the mutual influence of the difference of the ascending nodes $\Delta\Omega$, the eccentricity difference Δe, and the inclination difference Δi is the additional small along-track baseline ΔB^L_{along} in (13) that has been derived from Fig. 8. It causes a polar angle different from zero at the central orbit position COP at perigee or apogee. It can be corrected by a small phasing of the measurement orbit equivalent to a small orbit time-shift $\Delta\tau$. With v_s being the measurement satellite's velocity at the respective COP, $\Delta\tau$ is calculated by (20).

$$\Delta\tau = -\Delta B^L_{along} \cdot v_s \tag{20}$$

Fig. 12 (a) provides a summary of the Double-Cross-Helix orbit parameters calculation so far. It shows the calculation sequence of the differential orbit parameters, which are required to measure the radar satellite's antenna pattern at a desired azimuthal cut angle ξ_{cut}.

Due to the approximations in the derivation of the differential orbit parameters, small deviations occur at the central orbit position COP. First, the along-track baseline is not exactly zero.

Second, the measurement satellite is not exactly in the main radar antenna illumination direction w.r.t. the side-looking offset angle θ_{off}.
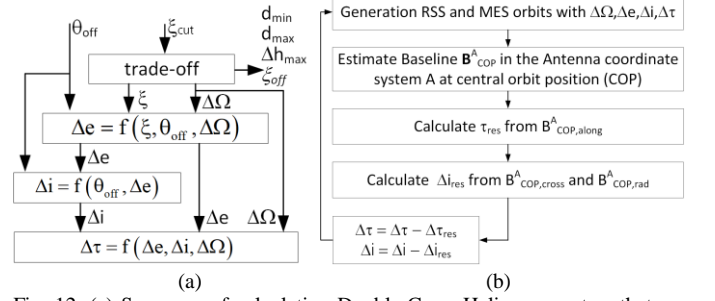

Fig. 12. (a) Sequence of calculating Double-Cross-Helix parameters that are required to measure a polar angle span at a desired fixed azimuthal cut angle ξ_{cut}, which is input to the calculation as well as the side-looking offset angle θ_{off}. The trade-off from the previous Section IV.D results in a value for the *fixed* difference in the ascending nodes $\Delta\Omega$, an azimuthal offset angle ξ_{off}, and an azimuthal angle ξ. The minimum and maximum distances d_{min} and d_{max} as well as the maximum difference in the orbit's altitude Δh_{max} is varied in the trade-off until a suitable value for $\Delta\Omega$ is found. Next, the difference in the eccentricities Δe is calculated, followed by the inclination difference Δi, and finally the small phasing orbit time-shift $\Delta\tau$. (b) Numerical fine adjustment to compensate for necessary approximations in the calculation of the differential orbit parameters.

To account for these small deviations, the numerical fine adjustment in Fig. 12 (b) is carried out in a few iterations. In a first step, the radar and measurement satellites orbits are generated. Then the baseline vector $\mathbf{B}^A$ is calculated in the *Antenna* system with the equations of Section III.B at the central orbit position COP. Its along-track component is approximately converted into a residual phasing orbit-time $\Delta\tau_{res}$ of the measurement orbit with the first line of (21). Following (15), a residual elevation angle $\theta_{el,res}$ is calculated in the second line of (21), and with (17) converted into a residual inclination Δi_{res}. Then $\Delta\tau$ and Δi are updated for the next iteration as is shown in Fig. 12 (b) using these residual values. For the high-level system concept parameters, the residual deviations $\Delta\tau_{res}$ and Δi_{res} at the central orbit position COP after 5 iterations are in the order of 10^{-8} s and 10^{-10} °, respectively.

$$\Delta\tau_{res} \approx B^A_{COP,along} / v_s$$

$$\theta_{el,res} = \text{asin}\left(\frac{-B^A_{COP,cross}}{\sqrt{\left(B^A_{COP,cross}\right)^2 + \left(B^A_{COP,rad}\right)^2}} \right) \tag{21}$$

$$\Delta i_{res} \approx \text{asin}\left(-\frac{\tan\theta_{el,res} \cdot \Delta e}{1 \mp (e_{RSS} + \Delta e)} \right)$$

V. ORBIT PARAMETER OF HIGH-LEVEL SYSTEM CONCEPT

Based on the equations of the previous Section, the Double-Cross-Helix parameters are calculated for the high-level system concept in steps of 10° of azimuthal angle. As is described in Section IV.C, the difference in the ascending nodes $\Delta\Omega$ is set to 0.065° for a desired minimum distance d_{min} of 1.8 km. The applied azimuthal offset angles ξ_{off} are the ones provided in Fig. 9 (b) in purple color together with the desired azimuthal cut angles ξ_{cut} in red color, and the resulting azimuthal angles ξ in black color. The values of the azimuthal offset angles ξ_{off} are 25°, 15°, 5° 0°, -5°, -15°, and 25°. The calculation of the

eccentricity differences Δe, the inclination differences Δi, and the phasing orbit-times of the measurement orbits $\Delta \tau$ was carried out in the sequence of Fig. 12(a) with the equations of Section IV. The resulting measurement satellite orbit parameters are exposed in Fig. 13 (b)-(d). For completeness, Fig. 13 (a) shows the constant difference in the ascending nodes.
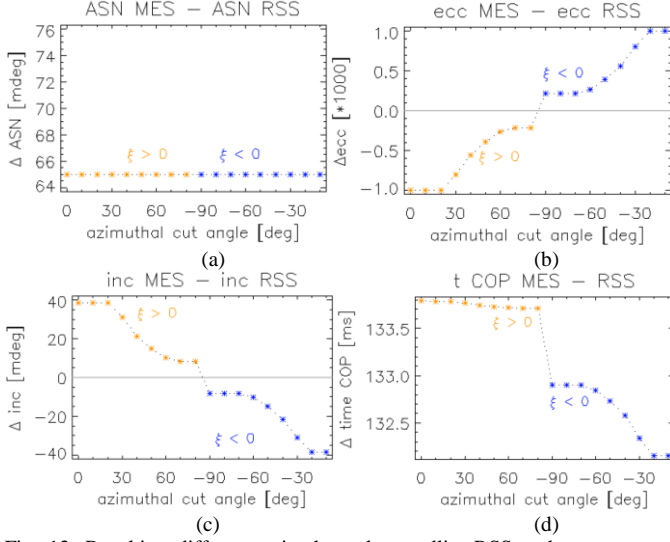

Fig. 13. Resulting differences in the radar satellite RSS and measurement satellite MES orbit parameters. The values for azimuthal angles $\xi < 0$ are in blue color, the ones for $\xi > 0$ are in orange color. Differences in (a) ascending nodes (fixed), (b) eccentricities, (c) inclinations, and (d) orbit time at central orbit position (COP).

Using the calculated orbit parameters, the orbits of radar and measurement satellites were generated and the measurement satellite's position was transformed into a baseline vector $\mathbf{B}^L(u)$ in the *Local* system of the radar satellite and its correspondence $\mathbf{B}^A(u)$ in the *Antenna* system. The components of these baseline vectors are provided in Fig. 14 together with the absolute value of $\mathbf{B}$, which equals to the distance d between the two satellites. In the plots (a)-(d), the curves of the largest and smallest azimuthal angles ξ are labeled.

Due to the selected azimuthal offset angles ξ_{off} (cf. Fig. 9b), the azimuthal angle ξ is identical for several azimuthal cut angles ξ_{cut}. This means identical measurement orbits in the *Local* system. In the *Antenna* system, the baselines are different due to the different azimuthal offset angles ξ_{off} that transform the *rotated* system into the final *Antenna* system.

Fig. 14 (c) shows that in the *Local* system at the equator, the cross-track baseline $B^L_{cross,\Delta\Omega,max}$ due to the ascending node difference $\Delta\Omega$ is 7.75 km for all azimuthal cut angles ξ_{cut}. This value results from (12) and is indicated by a grey line.

Fig. 14 (b) and (d) show the resulting baseline components in the *Antenna* system. As was the intention, at the central orbit position COP at perigee for $\xi < 0$ and apogee for $\xi > 0$, the radial baseline is positive and larger than zero, which means the measurement satellite faces the radar antenna. Likewise, the along-track baseline and the cross-track baseline are both zero, the latter consisting of the two components induced by a difference in the ascending nodes $\Delta\Omega$ and an inclination difference Δi. The courses of the *Local* system cross-track

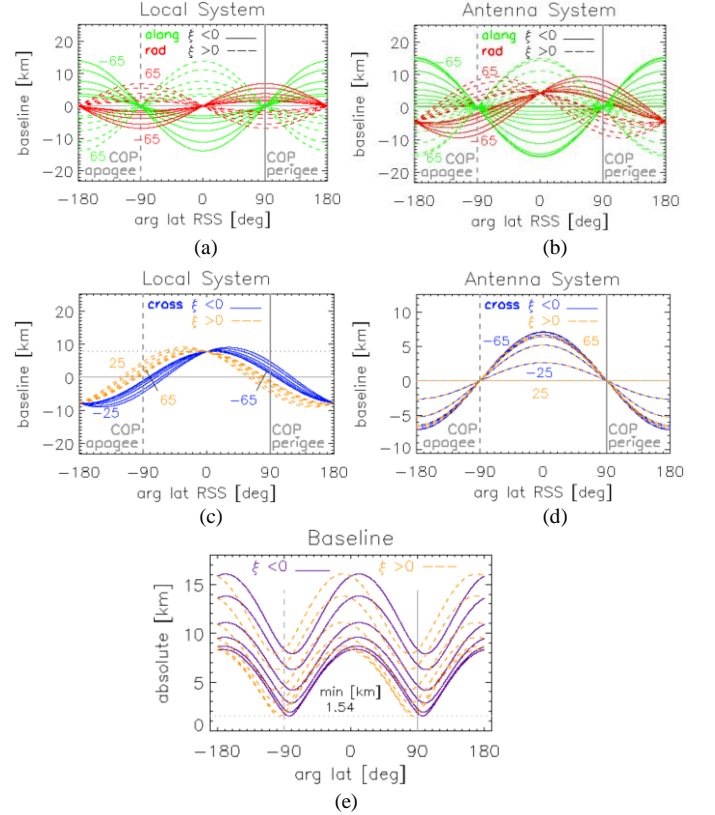baselines in Fig. 14 (c) correspond qualitatively to those of Fig. 6 (b) in dark blue color.

Fig. 14. (a)-(d) Baseline components in the *Local* and *Antenna* coordinate systems of the radar satellite RSS for different azimuthal angles ξ. Largest and smallest positive and negative azimuthal angles ξ are labeled. (e) The absolute values of the baseline vectors. The overall minimum d_{min} of 1.54 km is indicated by a horizontal line.

Fig. 14 (e) shows the absolute values of the baseline vectors $\mathbf{B}$, i.e. the distance d, for the different azimuthal angles ξ, and indicates the overall minimum distance d_{min} of 1.54 km. The maximum distance d_{max} is 16.06 km. The trade-off in Section IV.C started with a d_{min} of 1.8 km and led to a d_{max} of 15.8 km. The small deviations are due to the approximated formulas that assumed d_{min} and d_{max} at $u = \pm 90°$ and $u = 0°$. As can be seen in plot (e), the minimum and maximum values are not exactly at these orbit positions. This displacement corresponds to the small orbit-time shift $\Delta\tau$ of equation (20).

From the baseline components in the *Antenna* system, the azimuthal ξ and polar ψ measurement angles were calculated at each orbit position using (3). Simultaneous signal power measurements provide the central cuts through the two-dimensional antenna pattern.

The azimuthal cut angles in plot Fig. 15 (a) and the polar angles in plot (b) are versus argument of latitude and indicate the orbit Sections where the antenna pattern measurements are taken. Measurements are considered for positive values of the radial component of $\mathbf{B}^A$, i.e. in the case the measurement satellite faces the front of the radar antenna. Fig. 17 demonstrates that the desired azimuthal cut angles can be obtained from the measurement orbits that result from the calculated Double-Cross-Helix orbit parameters.
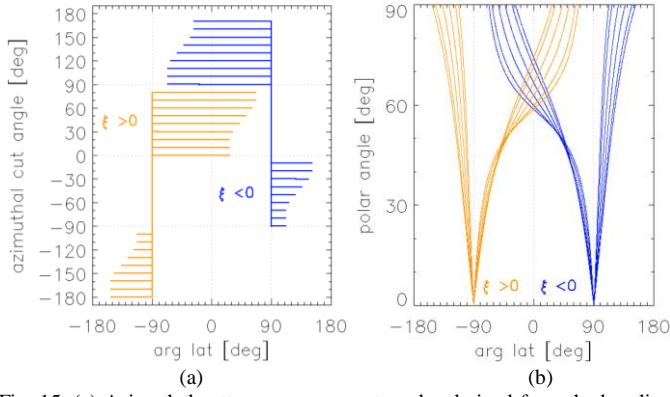
Fig. 15. (a) Azimuthal pattern measurement angles derived from the baseline components in the radar satellite's *Antenna* system. Those orbit positions are plotted where the measurement satellite faces the front of the radar antenna. The colors indicate an azimuth angle $\xi < 0$ (blue) and $\xi > 0$ (orange). (b) Corresponding polar angles in the same color coding.

A. Antenna Pattern in Azimuth/Elevation Angle Representation

The high-level system concept is a Synthetic Aperture Radar SAR. In SAR, the representation of the antenna pattern in azimuth and elevation angles is most relevant - from overall system design to image generation, e.g. [19].

Fig. 16 shows, again in the radar satellite's *Antenna* system (cf. Fig. 5), the antenna azimuth and elevation angles θ_{az} and θ_{el}, respectively. Fixing either the azimuth or the elevation angle provides one-dimensional cuts through the antenna pattern. In case of a central cut through the antenna's main beam direction, these two cuts are denoted by elevation and azimuth pattern, respectively.

As well as the azimuthal ξ and the polar ψ angles, the azimuth and the elevation angles can be obtained from the components of the baseline vector in the *Antenna* system. In contrary to ξ and ψ, the azimuth angle θ_{az} and the elevation angle θ_{el} are not part of a spherical coordinate system. There is only an unambiguous relation from the baseline components in along-track, cross-track and radial direction B^A_{along}, B^A_{cross}, and B^A_{rad}, respectively, to the azimuth angle θ_{az} and elevation angle θ_{el}, if the sequence of rotations is defined as well. For this paper, a vector pointing into z^A-axis direction is first rotated by the elevation angle θ_{el} around the x^A-axis, and then the resulting vector is rotated by the azimuth angle θ_{az} around the y^A-axis. For visualization, Fig. 16 shows also a rotation of the whole x^A-z^A-plane by the elevation angle θ_{el}.
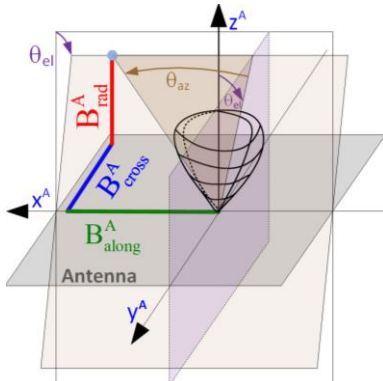

Fig. 16. Antenna pattern with azimuth angle θ_{az} and elevation angle θ_{el} in the radar satellite's *Antenna* coordinate system A. The selected sequence of rotation is first elevation angle θ_{el} and then azimuth angle θ_{az}.

Following the above rotation sequence, the equations of (22) provide the transformation from the *Antenna* system's baseline components into azimuth θ_{az} and elevation θ_{el} angles. The distance d is defined in (3).

$$\sin\theta_{el} = \frac{-B^A_{cross}}{\sqrt{\left(B^A_{cross}\right)^2 + \left(B^A_{rad}\right)^2}}$$

$$\sin\theta_{az} = \frac{B^A_{along}}{d \cdot \cos\theta_{el}} \tag{22}$$

From the baseline components in the *Antenna* system that are shown in Fig. 14 (b) and (d), the azimuth θ_{az} and elevation θ_{el} angles were calculated at each orbit position. The resulting antenna pattern cuts are provided in Fig. 17 (a) in the two-dimensional azimuth/elevation angle domain.
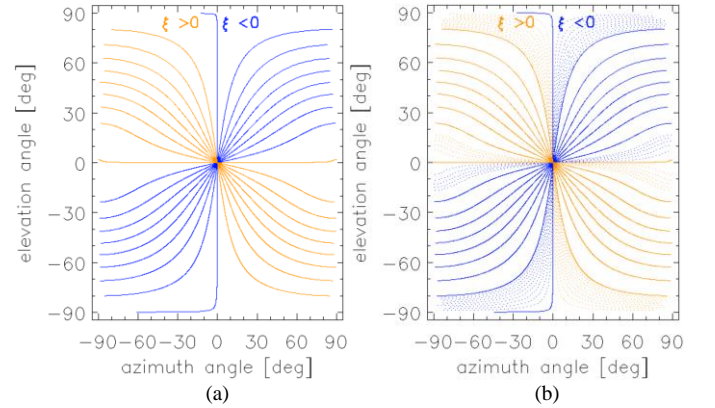

Fig. 17. (a) Locations of the antenna pattern cuts in the two-dimensional azimuth/elevation angle space. Same color coding as in Fig. 15. (b) Same plot for the drifted measurement approach that is discussed in Section VI.

VI. ASCENDING NODE DRIFT

For near-circular orbits, the secular variation rate of the ascending node $\dot\Omega$ can be well approximated based on the J_2-term of the geopotential [24]:

$$\dot\Omega \approx -\frac{3}{2} \cdot J_2 \cdot \sqrt{\frac{\mu}{a^3}} \cdot \left(\frac{r_{E,equator}}{a \cdot (1-e^2)}\right)^2 \cdot \cos i \tag{23}$$

with μ being the product of the gravitational constant and the Earth's mass, and $r_{E,equator}$ being the Earth's radius at the equator. The variation of Ω can be exploited to adjust a sun-synchronous orbit [24]. This is the case for the RSS orbit and the inclination i_{RSS} results from there to 97.455°. For the following analysis the term e^2 can be neglected since it is very small compared to 1.

The difference in the RSS and MES inclinations Δi causes different variation rates $\dot\Omega$ that cause a drift of the MES ascending node w.r.t. the RSS one. The difference in the drift rates $\Delta\dot\Omega$ is

$$\Delta\dot\Omega = \dot\Omega_{MES}\left(i_{RSS} + \Delta i\right) - \dot\Omega_{RSS}\left(i_{RSS}\right) \tag{24}$$

with $\dot\Omega_{MES}$ and $\dot\Omega_{RSS}$ being the drift rates of the MES and RSS satellites, respectively.

The following sub-sections discuss the effect of $\Delta\dot\Omega$. First, for the calculation approach of the Double-Helix-Parameters presented in Section V with a fixed difference in the ascending node $\Delta\Omega$, the deviation of this fixed value due to the drift rate

difference $\Delta\dot\Omega$ is quantified. Second, a variation of the Double-Helix-Parameters calculation approach is presented that exploits the drift rate difference $\Delta\dot\Omega$ for the antenna pattern measurement at the different azimuthal cut angles ξ_{cut}.

In the following, the calculation approach of Section V is denoted by *fixed $\Delta\Omega$*, and the variation that exploits the ascending node drift is denoted by *drifted $\Delta\Omega$*.

A. Deviation in Fixed $\Delta\Omega$ Parameter Calculation

From the inclination differences of Fig. 13 (c), the corresponding deviation from the fixed $\Delta\Omega$ value per orbit was estimated by using (24). Fig. 18 (a) shows the result on the left vertical axis. The right vertical axis provides a conversion into a cross-track baseline deviation at the equator. The maximum drift per measurement orbit is -0.33 mdeg that is 0.5% of the fixed $\Delta\Omega$ value of 65 mdeg, which corresponds to 7.2 km cross-track baseline at the equator.

The deviation is rather small and can be considered in the measurement satellite's orbit parameter calculation by an adjustment of the *input* parameter $\Delta\Omega$ in Section V.A. However, the antenna pattern measurement should be carried out without longer delays between the individual measurement orbits. Otherwise, the deviations from the fixed ascending node difference $\Delta\Omega$ requires corrections by orbit maneuvers.

B. Parameter Calculation with Drifted $\Delta\Omega$

The drift effect of the ascending node due to the inclination difference Δi can also be useful in the orbit parameter calculation. This is accompanied by an increase of the measurement time, but gets by with a reduction of the required ΔV for a full two-dimensional antenna pattern measurement, independent off the sampling density of the azimuthal angle. The eccentricity and inclination differences Δe and Δi are fixed, and depending on the drifting rate difference $\Delta\dot\Omega$, the desired azimuthal angles ξ adjust after particular times.

The derivation of the dependency of the azimuthal angle ξ from the ascending node difference $\Delta\Omega$ starts with an approximation of (17) into a linear relation between the differences in eccentricity Δe and inclination Δi:

$$\Delta i \approx -\tan\theta_{off}\cdot\Delta e \quad\Rightarrow\quad \frac{\Delta i}{\Delta e}\approx -\tan\theta_{off} \tag{25}$$

Then, the approximation of $\sin(\Delta\Omega)$ by $\Delta\Omega$ in (16) and insertion of (25) provides:

$$\tan\xi \approx \frac{\sin(i_{RSS})\cdot\left(1-e_{RSS}^2\right)\cdot\sin\theta_{off}}{2}\cdot\frac{\Delta\Omega}{\Delta i} \tag{26}$$

The difference in the drift rates $\Delta\dot\Omega$ in (24) can be approximated by:

$$\Delta\dot\Omega = k_\Omega\cdot\left[\cos(i_{RSS}+\Delta i)-\cos i_{RSS}\right]\approx k_\Omega\cdot\Delta i$$

with $\left[\cos(i_{RSS}+\Delta i)-\cos i_{RSS}\right]\approx\left(2-\left(i_{RSS}-\frac{\pi}{2}\right)^2\right)\cdot\Delta i$

$$\tag{27}$$

and $k_\Omega = +\frac{3}{4}\cdot J_2\cdot\sqrt{\frac{\mu}{a^3}}\cdot\left(\frac{r_{E,equator}}{a\cdot\left(1-e_{RSS}^2\right)}\right)^2\cdot\left(2-\left(i_{RSS}-\frac{\pi}{2}\right)^2\right)$

Then, $\Delta\Omega$ is split into a start value $\Delta\Omega_{start}$ and a drifting part

$$\Delta\Omega = \Delta\Omega_{start}+\Delta\dot\Omega\cdot T_{orbit}\cdot n_{drifted} \tag{28}$$

with T_{orbit} being the orbit period and $n_{drifted}$ being the number of drifted orbits from measurement start to current measurement, the azimuthal angle ξ in (26) becomes

$$\tan\xi\left(n_{drifted}\right)\approx\frac{\sin(i_{RSS})\cdot\left(1-e_{RSS}^2\right)\cdot\sin\theta_{off}}{2}\cdot\frac{\Delta\Omega_{start}+\Delta\dot\Omega\cdot T_{orbit}\cdot n_{drifted}}{\Delta i} \tag{29}$$

In the following, the approximation is made that the difference in the ascending nodes $\Delta\Omega$ is constant during an orbit, and its variation due to drift only happens once per orbit. The approximation can be made since the drift difference of the ascending nodes is relatively slow.

The first orbit parameter to be estimated is the starting value of the ascending node difference $\Delta\Omega_{start}$ that results from the desired minimum distance d_{min} and the assigned azimuthal offset angle $\xi_{off,\pm90°}$ (cf. (41)).

$$\sin\Delta\Omega_{start}\approx\frac{2\cdot d_{min}\cdot\tan|\xi_{start}|}{a\cdot\sin i_{RSS}}=\frac{2\cdot d_{min}\cdot\tan\left|-90°+\xi_{off,-90°}\right|}{a\cdot\sin i_{RSS}} \tag{30}$$

For better comparability, d_{min} and the azimuthal offset angles (cf. Fig. 9 b) of the previous calculation with *fixed* ascending node difference $\Delta\Omega$ continues to be used also for the *drifting* case discussed here. Next, the required inclination difference Δi follows by setting $n_{drifted}$ in (29) to zero

$$\Delta i\approx\frac{\Delta\Omega_{start}\cdot\sin(i_{RSS})\cdot\left(1-e_{RSS}^2\right)\cdot\sin\theta_{off}}{2\cdot\tan\xi_{start}} \tag{31}$$

The eccentricity difference Δe is coupled via the mechanical offset angle θ_{off} to the inclination difference Δi, and is obtained from (17) with the upper signs for $\xi<0$ and the lower signs for $\xi>0$.

$$\Delta e\approx\frac{-\sin\Delta i\cdot\left(1\mp e_{RSS}\right)}{\tan\theta_{off}\mp\sin\Delta i} \tag{32}$$

The number of drifted orbits $n_{drifted}(\xi)$ until $\Delta\Omega$ adjusts for the measurement of a desired azimuthal angle ξ is derived from (29)

$$n_{drifted}\left(\xi\right)=\frac{2\cdot\left(\tan\xi-\tan\xi_{start}\right)}{\sin(i_{RSS})\cdot\left(1-e_{RSS}^2\right)\cdot\sin\theta_{off}\cdot k_\Omega\cdot T_{Orbit}} \tag{33}$$

Note that in the derivation the dependency of Δi vanishes for ξ but is present in ξ_{start}. This means that the duration of a two-dimensional measurement is with the above approximations independent off Δi, or rather from its absolute.

The final adjustments are identical to the *fixed $\Delta\Omega$* calculation in Section IV.D. The small phasing of the measurement orbit equivalent to a small orbit time-shift $\Delta\tau$ to correct for the central orbit position COP at perigee or apogee is calculated by (20). Finally, the same numerical fine adjustment in Δi and $\Delta\tau$ is executed as described in Fig. 12 b.

C. High-Level System Concept Parameters Calculated with Drifted $\Delta\Omega$

The same azimuthal cut angles ξ_{cut} in steps of 10°, and the same azimuthal offset angles ξ_{cut} (cf. Fig. 9 b) as for the *fixed $\Delta\Omega$* calculation approach were simulated for the *drifted $\Delta\Omega$* approach. Since the minimum distance d_{min} and the assigned azimuthal offset angles $\xi_{off,\pm90°}$ were selected identical to the *fixed $\Delta\Omega$* calculation, the starting value of the ascending node difference $\Delta\Omega_{start}$ results to the same 65 mdeg that were selected for the *fixed $\Delta\Omega$* calculation in Section IV.C.

The number of drifted orbits $n_{drifted}$ until $\Delta\Omega$ adjusts for the measurements is provided Fig. 18 (b) versus the azimuthal cut angle ξ_{cut}. The comparison with Fig. 19 (a), which provides the difference in the ascending nodes $\Delta\Omega$ required for the measurement at dedicated ξ_{cut} angles, reveals the sequence of measurements. This sequence is requiring the smallest change in the differential orbit parameters and is thus better in terms of required ΔV. With $\Delta\Omega_{start} = 65$ mdeg, the ξ_{cut} angles from -90° to -70° are measured in successive orbits, then about 200 orbits later, the measurement at $\xi_{cut} = -60°$ takes place. Before the measurement at $\xi_{cut} = 0°$, an orbit maneuver changes the sign of the difference in inclination Δi and eccentricity Δe as is shown in Fig. 19 (b) and (c). The sign change in Δi reverts the direction of the difference in the ascending node drifts and the measurements at the positive ξ_{cut} angles can start. After 93 days, a full two-dimensional measurement is completed. It is reasonable to start a next measurement in reversed sequence starting with positive ξ_{cut} angles, without an additional orbit maneuver. Again, after measuring $\xi_{cut} = 0°$, the signs of Δi and Δe are switched.
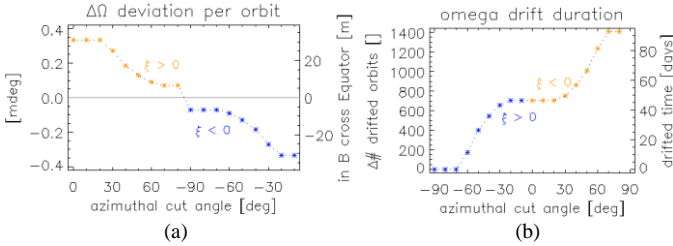

Fig. 18. (a) Fixed $\Delta\Omega$-Approach. Deviation from the fixed $\Delta\Omega$ value per orbit due to the difference in the ascending node drifts of measurement (MES) and radar (RSS) satellites. (b) Drifted $\Delta\Omega$-Approach. Number of drifted orbits until the difference in the ascending nodes $\Delta\Omega$ adjusts for the measurements of at dedicated azimuthal cut angles ξ_{cut}. Due to the azimuthal offset angles ξ_{off} (cf. Fig. 9 b), the same azimuthal angle ξ is used for several ξ_{cut} angles. This causes the horizonal course of the curve in some sections, e.g. from -90° to -70° azimuthal cut angle.

Fig. 19 provides the differences in the orbit parameters of the measurement satellite MES w.r.t. the radar satellite RSS for the drifted $\Delta\Omega$–approach. In contrast to Fig. 13, the differences in eccentricity Δe and inclination Δi are, apart from the sign-change constant, and the difference in the ascending nodes varies. The orbit time $\Delta\tau$ at central orbit position COP in Fig. 19 (d) depends on the difference in the ascending nodes $\Delta\Omega$ (cf. (13), (20)), and thus shows a larger variation with ξ_{cut} as it was the case in Fig. 13.

Fig. 20 provides the resulting baseline components in the local and the antenna systems. In can be compared with Fig. 14 for the fixed calculation approach. The local system along and radial baselines follow two curves only, one for azimuthal angles ξ above 0° and one for ξ below. This is due to the constant differences in eccentricity Δe. Since the difference in the ascending node varies $\Delta\Omega$, the cross-track baseline in plot (c) follows different curves. The reduction of the radial and along-track local system baselines causes also a decrease of the absolute of the baselines in plot (e) compared to Fig. 14.

The resulting azimuthal cut ξ_{cut} and polar ψ measurement angles are identical to the ones of the fixed $\Delta\Omega$ measurement approach that already are provided in Fig. 15. The same holds

for the locations of the antenna pattern cuts in the two-dimensional azimuth θ_{az} and elevation θ_{el} angles measurement angle space. For completeness, the azimuth/elevation angle plot for the drifted measurement approach discussed in this section, is added in Fig. 17 (b).
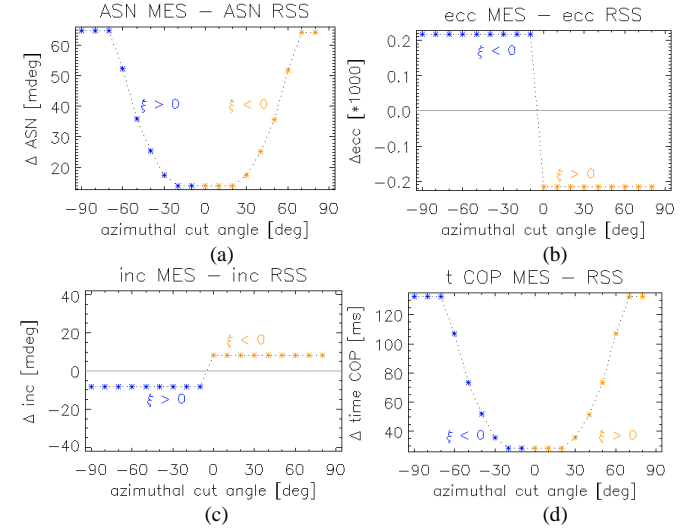
Fig. 19. Drifted $\Delta\Omega$-Approach. Differences in the radar RSS and measurement satellites MES orbit parameters. (a) Ascending nodes, (b) eccentricities, (c) inclinations, and (d) orbit times at central orbit position COP.

D. Comparison of Fixed $\Delta\Omega$ and Drifted $\Delta\Omega$ Approaches

The fixed $\Delta\Omega$ approach provides the two-dimensional measurement in shorter time. In case of 10° azimuthal cut angle steps and with the assumption of an update of the measurement orbit parameters in each orbit, the measurement lasts 18 times the orbit period, i.e. 29 hours. The duration of the drifting $\Delta\Omega$ approach in the example is 93 days.
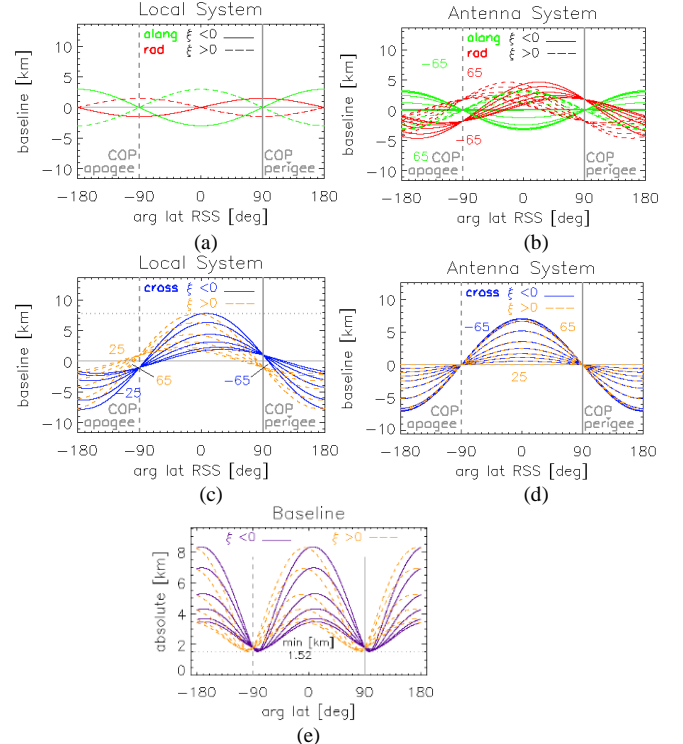
Fig. 20. Drifted measurement approach. (a)-(d) Baseline components in the *Local* and *Antenna* coordinate systems. (e) The absolute values of the baseline vector, i.e. the distances between the satellites.

A finer sampling of the azimuthal cut angle ξ_{cut} increases the duration of the fixed $\Delta\Omega$ approach but does not increase the duration of the drifted $\Delta\Omega$ approach. The required ΔV for the orbit maneuvers of the measurement satellite MES does not increase in both approaches for an increased ξ_{cut} sampling.

The ΔV for the fixed $\Delta\Omega$ approach is generally higher due to more active maneuvers for changing the measurement orbits. For the drifting $\Delta\Omega$ approach only one considerable maneuver is required to switch the signs of Δi and Δe in one full two-dimensional measurement. A first order and not optimized analysis of the required ΔV was performed based on separated changes of the orbit parameters in Fig. 13 and Fig. 19. It is expected that a more elaborated and combined maneuver strategy will reduce the required ΔV. However, Fig. 21 provides the estimate for both approaches. Note the difference in the measurement sequences for more economical ΔV.
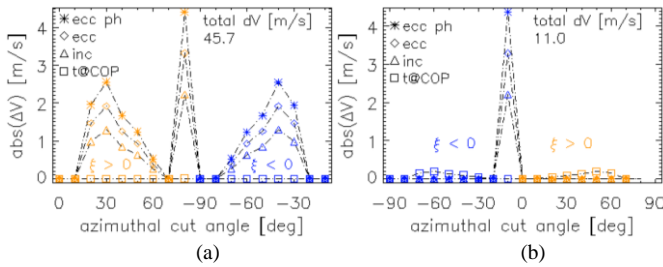

Fig. 21. Required ΔV for changing the measurement orbits for the fixed $\Delta\Omega$ approach (a) and the drifting $\Delta\Omega$ approach (b). The individual ΔV contributions for changing the eccentricity, the orbit phasing due to an eccentricity change, the inclination, and the phasing for equalizing the times at central orbit position COP are indicated by different symbols.

The total ΔV for one two-dimensional measurement is about 45 m/s for the fixed $\Delta\Omega$ approach, and 11 m/s for the drifted $\Delta\Omega$ approach. The drifted $\Delta\Omega$ approach requires only one larger maneuver for the sign switching.

The minimum distance d_{min} between the radar RSS and the measurement satellite MES is above 1.5 km for both approaches, but the maximum distance for the drifted $\Delta\Omega$ approach is with 8.3 km about half that of the 16 km of the fixed $\Delta\Omega$ approach. The maximum difference in the orbit altitude is 1.5 km for the drifted $\Delta\Omega$ approach and about 7 km for the fixed $\Delta\Omega$ approach.

VII. HIGH-LEVEL SYSTEM CONCEPT - MEASUREMENT ACCURACY AND ANGULAR SAMPLING

The high-level system concept of Section II is complemented by a measurement gain and pointing error analysis. The angular sampling distance is discussed based on the Double-Cross-Helix orbits that were calculated in the previous Section V.

A. Accuracy of Pattern Gain Measurement

A first order error analysis of the measurement gain is provided with contributions from noise and relative measurement distance deviation. The assumption is made that the reflecting sphere can be fabricated accurately enough to avoid significant RCS variations. As mentioned in the beginning of section II, the reflecting sphere should always be oriented towards the RSS antenna. The gain error due to noise $\Delta G_{err,SNR}$ is estimated from the $SNR_{RC,AC}$ in (2), which relates the

noise power P_N to the measurement signal power after range and azimuth compression $P_{S,RC,AC}$, which depends on the distance d. The noise power P_N is constant with d, and the gain error due to noise can be expressed by

$$\Delta G_{err,SNR} = \frac{P_{S,RC,AC} + P_N}{P_{S,RC,AC}} = 1 + \frac{1}{SNR_{RC,AC}} \tag{34}$$

For the high-level system concept, $\Delta G_{err,SNR}$ is shown in Fig. 22 (a), in blue color for the pattern peak since $P_{S,RC,AC}$ in (2) is calculated for the maximum antenna pattern gain. It is due to the increasing number of azimuth pulses that the $SNR_{RC,AC}$ is kept above 35 dB for increasing distance d and thus, $\Delta G_{err,SNR}$ remains below 0.001 dB. The serrated shape of the curve is due to the integer number of azimuth pulses. In red color, Fig. 22 (a) also provides the gain error at the edge of the typically processed antenna pattern, i.e. -6 dB below the peak of the two-way pattern. For an assumed local pattern gain maximum at the first sidelobe's peak of -26.4 dB below the two-way gain maximum, the gain error contribution due to noise is 0.6 dB. The pattern around the first sidelobes is of particular importance for ambiguity calculations, e.g. [20],[21].

The knowledge of the relative measurement distance error also contributes to the error of the antenna pattern gain. Fig. 22 (a) shows in orange color the distance error contribution in the signal power equation (1) assuming a 5 cm knowledge of the relative radar and measurement satellites distance d.

In this paper we assume the same viewing angle from the reflecting sphere towards the RSS antenna at all orbit positions. Even if the absolute RCS of the reflecting sphere is not known perfectly, it is very constant due to the steering of the sphere always towards the RSS satellite. Additionally, before launch, the RCS of the reflecting sphere with the MES bus structure can be measured to estimate the absolute RCS and the RCS variations versus the viewing aspect. These measurements can be used to correct residual viewing angle variations.
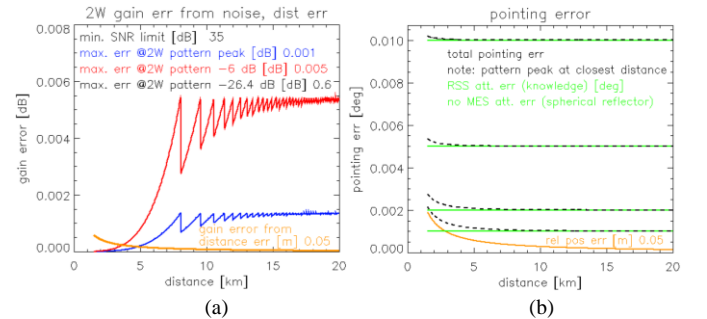
Fig. 22. (a) Measurement gain error contribution from noise at the peak of the two-way pattern (blue), and at the edge of the processed antenna pattern (red). The gain error for the peak of a first sidelobe at -26.4 dB below the two-way main lobe peak is 0.6 dB. The gain error due to an assumed relative distance error knowledge of 5 cm (orange). (b) Total pointing error (black), and the contributions of relative position error knowledge (orange) and the different considered radar satellite attitude error knowledges (green).

B. Angular Accuracy of Pattern Measurement

The angular accuracy of the pattern measurement is estimated with the following assumptions:

- A 5 cm knowledge of the relative satellite's position error Δpos is assumed, and approximately converted into a pointing error ε_{pos} that decreases with distance d by

$$\varepsilon_{pos} \approx \operatorname{atan}\left(\frac{\Delta pos}{d}\right) \tag{35}$$

- The radius of the reflecting sphere r_r is much larger than the wavelength λ and thus well in the optical region. The ratio $2\cdot\pi\cdot r_r/\lambda$ is 30, and the optical region starts at a ratio of 10 following [18]. A deviation of the direction of the reflected signal from the incident signal is thus not considered.

- The following radar satellite's attitude knowledge error assumptions were analyzed: 0.001°, 0.002° (measured pointing knowledge in TerraSAR-X [3]), 0.005° (specified pointing knowledge of ROSE-L [26]), and 0.01°. Due to the shape of the reflecting sphere the measurement satellite's attitude error is neglected.

Fig. 22 (b) provides the resulting total pointing error in black, and the contributions of relative position error knowledge and the different radar satellite's attitude error knowledges in orange and green colors, respectively, as function of distance d. The radar satellite's pointing accuracy is driving to a great part the total pointing accuracy of the measurement.

The time-variant distance between the RSS and MES can be estimated on-ground when the precise post-flight orbit data from both satellites have been calculated on-ground. The same holds for the precise post-flight attitude data. The precise orbit and attitude data derive usually from the GNSS and star sensor data in the telemetry.

C. Polar Angle Sampling Distance

Based on the Double-Cross-Helix orbits and the high-level system concept, the polar angle sampling is discussed.

A dense angular sampling of the antenna pattern central cuts is desirable, i.e. a short sampling interval. On the other hand, several measurement pulses, i.e. a burst of pules, may be sent at a quasi-fixed angular position for high gain measurement accuracy (cf. varying azimuth compression length in Section II). So, the length of a burst needs to be discussed w.r.t. the length of a sampling interval.

Fig. 23 (a) symbolizes several bursts of measurement pulses in green color. The time interval between measurement pulses in one burst is the Pulse Repetition Interval $PRI = 1/PRF$, i.e. 0.147 ms for the high-level system concept. The time length of the bursts $TB_{Length}(u)$ results from the number of azimuth pulses that are required to achieve a minimum SNR (cf. Fig. 2 (b)) and thus varies with argument of latitude u.

The time intervals between the measurement bursts $TB_{Interval}$ correspond to polar angle sampling distances in degree. Due to the orbit geometry, equidistant time intervals $TB_{Interval,const}$ mean varying polar angle sampling distances $\Delta\psi(u)$. Fig. 23 (b) shows for equidistant orbit time intervals $TB_{Interval,const}$ of 30 s the corresponding polar angle sampling positions versus argument of latitude u. The varying angular sampling distance can be observed. In order to obtain a constant angular sampling distance $\Delta\psi_{const}$, the burst intervals $TB_{Interval}$ need to be adapted depending on u. This can be calculated by

$$TB_{Interval}(u) \approx TB_{Interval,const} \cdot \Delta\psi_{const} / \Delta\psi(u) \tag{36}$$

where $\Delta\psi(u)$ and $TB_{Interval,const}$ can be obtained from an orbit calculation with constant time sampling, as was also done for Fig. 23 (b).

For a desired dense angular sampling distance $\Delta\psi_{const}$ of 0.01°, the resulting burst interval $TB_{Interval}(u)$ is shown in Fig. 23 (c) together with the burst length $TB_{Length}(u)$ for the azimuthal angle ξ of -25° and a SNR of 35 dB. Fig. 23 (d) provides the difference for a ξ of -65°, the *worst case* with the smallest absolute separation between burst interval and burst length. This time gap is available for concurrent patterns measurement at identical azimuthal angle ξ and identical measurement orbit. On the other hand, the time gap indicates the densest possible polar angle sampling for measuring only one antenna pattern. Dividing the minimum time gap for $\xi = -65°$ of 28.83 ms by the burst length at that minimum of 0.15 ms, the number of patterns that could be measured concurrent is 196. The densest polar angle sampling in case of measuring only one pattern is 0.9 μdeg.

The concurrent pattern measurement is possible due to the relatively slow variation of the baselines along one measurement orbit that provides one central cut. It is very advantageous for systems with many different patterns and/or feed-array elements that are electronically switched. For example, TerraSAR-X [1] combines electronic steering in azimuth and elevation that results in more than 20000 different antenna patterns. Another example is the Tandem-L proposal [25] with its feed array with 35 elevation and 6 azimuth elements. All the individual feed elements can be switched in a sequence and thus be measured quasi in-parallel in the same orbit.
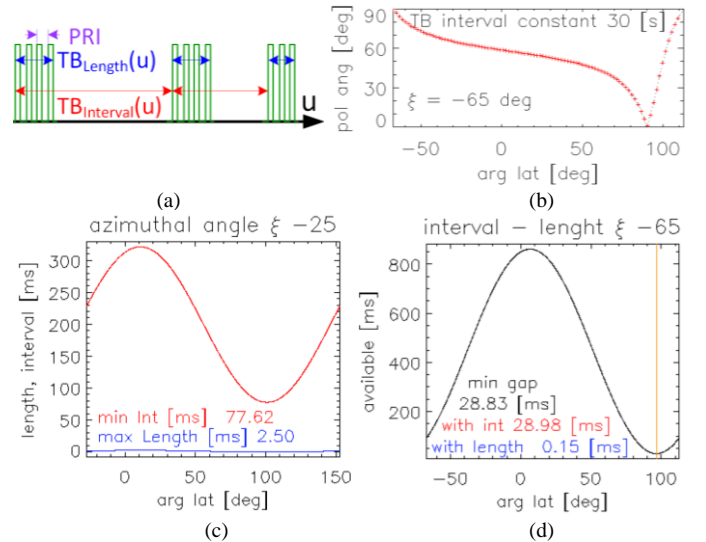
Fig. 23. (a) Pulses of a measurement burst (green). Burst length (blue) varies with argument of latitude u for a constant minimum SNR. Burst interval (red) varies with u for a constant angular polar angle sampling distance. (b) Polar angle measurement positions for orbit simulation with a measurement interval $TB_{Interval,const}$ fixed to 30 s. The polar angle curve is for an azimuthal angle of -65° and is identical to the one in plot (b) of Fig. 15. (c) Measurement burst length and measurement burst interval for the azimuthal angle $\xi = -25°$ with a minimum SNR of 35 dB and a constant polar angle sampling $\Delta\psi(u)$ of 0.01°. (d) Difference between burst length $TB_{Length}(u)$ and burst interval $TB_{Interval}(u)$ for measurement of $\xi = -65°$. The minimum, indicated by the vertical line, can be used to calculate the maximum number of concurrent measurements of the same azimuthal angle cut of different antenna patterns in one identical orbit.

VIII. Discussion

The minimum required cooperation from the radar satellite is to transmit and receive a measurement signal to and from the measurement satellite at specified times. The radar satellite does not need to change its orbit, but a small update of the usually available attitude steering is required.

The high-level system concept considers a two-way pattern measurement. However, by equipping the measurement satellite with a transmitter and a receiver, and/or a transponder the one-way pattern in Tx and Rx can be measured as well.

A two-dimensional measurement can be done within few days in case of a LEO satellite. This is much faster than the one-dimensional on-ground measurements performed by calibration targets that are moreover only available in azimuth or elevation direction. The proposed method allows thus also for shorter maintenance intervals. On the other hand, a one-dimensional azimuth or elevation pattern measurement of the main lobe can be obtained within one orbit by the proposed Double-Cross-Helix method.

The Double-Cross-Helix orbit allows for a two-dimensional antenna pattern measurement over a wide polar angle range that can be up to $\pm90°$. The measurement can even be extended to $\pm180°$, which means to include to the back side of the antenna, or rather the radar satellite.

The numerical adjustment allows for more sophisticated and realistic orbit models than Kepler orbits.

The modified yaw, pitch and roll angles should not become too large due to solar panel illumination and drag variations. This can be considered in the trade-off, too. The roll angle is considered to be the one with the strongest effect on the solar panel illumination. The effects of changes in yaw and pitch angle are considered to be small. On the other hand, in case of allowing also large updates of the attitude steering angles to realize large azimuthal offset angles, one sole measurement orbit can provide all azimuthal cut angles, which means no ΔV at all for the acquisition of all azimuthal cut angles of a two-dimensional antenna pattern measurement.

Electronically steered antenna patterns with main illumination directions different from the antenna system's z^A-axis can be measured as well. An electronical steering in elevation angle can be accounted for by a modification of the side-looking offset angle θ_{off} in the orbit parameter calculation. A pattern steered electronically in azimuth can be considered by incorporating the azimuth steering angle into the update of the radar satellite's attitude angles.

With a dense angular sampling, electronically steered antenna patterns can also be measured in the orbit configuration for the main illumination direction in-line with the *Antenna* system's z^A-axis. This is of special advantage if many different electronically steered beams should be measured. Since, even for dense measurement angle sampling, the required number of azimuth pulses per polar angle measurement position is small, the different antenna patterns can be electronically switched in one and the same measurement orbit. So, in only one orbit many different electronically steered patterns can be measured. This is also of great use in case of digital beamforming systems, e.g.

Tandem-L that is designed with many feed array elements that need individual pattern measurements, and the pattern characteristics is required highly accurate for a wide angular range, not only for the high gain part of the pattern main lobe.

In case of a distributed remote sensing system, i.e. several radar satellites fly in a formation, the measurement satellite can be part of the formation and measure the antenna pattern of all the formation satellites. In a remote sensing system with several radar satellites on Double-Cross-Helix orbits the radar satellites could even mutually measure their antenna patterns.

Since the measurement satellite is small it could be launched piggy-bag with a larger radar satellite to be already close to its required orbit. In case of several small radar satellites, the measurement satellite could be launched together with the formation.

In case of un-foldable RF antennas, the system budgets w.r.t. alignment stability before/after unfolding can be reduced since after unfolding, the resulting antenna pattern can be exactly measured in space.

Large antenna structures can often not be completely measured on-ground. Only parts of the antenna are then usually measured, and an antenna model is used to synthesize the pattern of the overall antenna. In such a case, the proposed approach can provide the measurement of the full antenna structure in space.

One of the greatest advantages of the in-orbit antenna pattern measurement by using the Double-Cross-Helix orbit formation is that the measurement is performed in free space with one free-flying measurement satellite. All distortions from atmosphere, ionosphere, ground clutter and multipath effects, ambiguities, volume scattering do not apply. Therefore, also the measurement of the antenna phase pattern is possible as well as an exact polarimetric antenna pattern measurement.

IX. Conclusions

The paper introduced the Double-Cross-Helix orbit formation and proposed an approach for the two-dimensional in-orbit measurement of a nadir-looking or side-looking spaceborne antenna by means of a small satellite that flies in Double-Cross-Helix formation.

By adjusting the Double-Cross-Helix parameters, one-dimensional central cuts through the two-dimensional pattern are obtained at adjustable azimuthal angle positions. The full two-dimensional pattern is obtained from numerous cuts at different azimuthal angle positions and, if necessary, an interpolation of these cuts.

A unique advantage is the possibility to measure the antenna pattern over a wide angular range, even at the satellite's rear, i.e., the side opposite the radar antenna.

The Double-Cross-Helix is mainly adjusted by differences in eccentricity Δe, ascending node $\Delta\Omega$, and inclination Δi, where the latter two generate two cross-track baseline components with maxima either at the equator or the perigee/apogee, respectively. A trade-off for estimating the difference in the ascending nodes $\Delta\Omega$ was provided that considers the distance variation between the satellites and the difference in the satellite orbit altitudes. Formulas were derived to calculate the required

differences in eccentricity *Δe* and inclination *Δi*.

A second order along-track adjustment by a phasing orbit-time *Δτ*, and a numerical adjustment were proposed to consider the approximations in the derivation of the Double-Cross-Helix orbit parameters.

An analysis was provided that defines whether the measurement at a desired azimuthal angle needs to be around a central orbit position COP at either apogee or perigee.

The concept of azimuthal offset angles was introduced, which first allows for exact one-dimensional azimuth and elevation pattern cuts, and second, minimizes the required changes of orbit parameters for the measurement at different azimuthal cut angles. It was shown that azimuthal offset angles can be realized by updating the yaw, pitch, and roll angles of the radar satellite.

Two different approaches for the calculation of the differential orbit parameters were introduced, one with fixed difference in the ascending nodes *ΔΩ* and one with drifted difference. The fixed approach is much faster and lasts few days, the drifted approach lasts months but requires less *ΔV*.

A high-level system concept was defined that consists of a side-looking SAR satellite and a small measurement satellite that carries a radar reflecting sphere. For this example, the system and orbit parameters were selected similar to the ones of the TerraSAR-X mission.

Power and *SNR* were analyzed for the high-level system concept. The power variation at the antenna output appears feasible by taking reference to a 3 m corner reflector at a slant range of 600 km. The *SNR* of the corner reflector after full range and azimuth compression is 35 dB. A partial moving range compression was proposed that allows for a frequency-dependent pattern measurement while improving the *SNR*, and maintaining the frequency dependence of the antenna pattern measurement. Additionally, an azimuth compression of a small number of pulses was proposed that keeps the *SNR* of the measurement signal above a desired value. The measurement gain and pointing errors were analyzed as well as the achievable angular sampling. A highly accurate measurement is possible at high angular sampling.

The operational implementation of an in-orbit two-way antenna pattern measurement requires a small satellite with a reflecting sphere, the commanding of the measurement satellite to fly in close formation, and the commanding of the radar satellite to update its attitude during the measurement orbits. With respect to the close formation flying, experience with more than 10 years of the TanDEM-X mission is available. The measurement of individual transmit and receive patterns requires an additional transmit/receive antenna on-board the measurement satellite, e.g. at the opposite side of the reflecting sphere, and for the receive pattern measurement the measurement signal needs to be sent to ground for evaluation. This can be realized most economically by an optical and phase preserving MirrorLink to the radar satellite [9]. This avoids the complete radar receive chain on board the measurement satellite and allows to use the one anyhow available on-board the radar satellite.

In future, the trend goes towards formations of small radar satellites, e.g. [27]-[29], and a small satellite in the formation can serve the formation with antenna pattern measurements. On the other hand, also for large constellations with individual stand-alone radar satellites, e.g. the large constellations being installed by the space industry, a dedicated small measurement satellite can serve one radar satellite of the constellation, and then move to the next radar satellite of the constellation.

APPENDIX A: PERIGEE/APOGEE MEASUREMENT

Fig. 24 illustrates how the sign of the eccentricity difference *Δe* determines whether the measurement must be carried out around the central orbit position COP either at perigee or apogee. The figure is for a right looking system with positive side-looking offset angle θ_{off}.
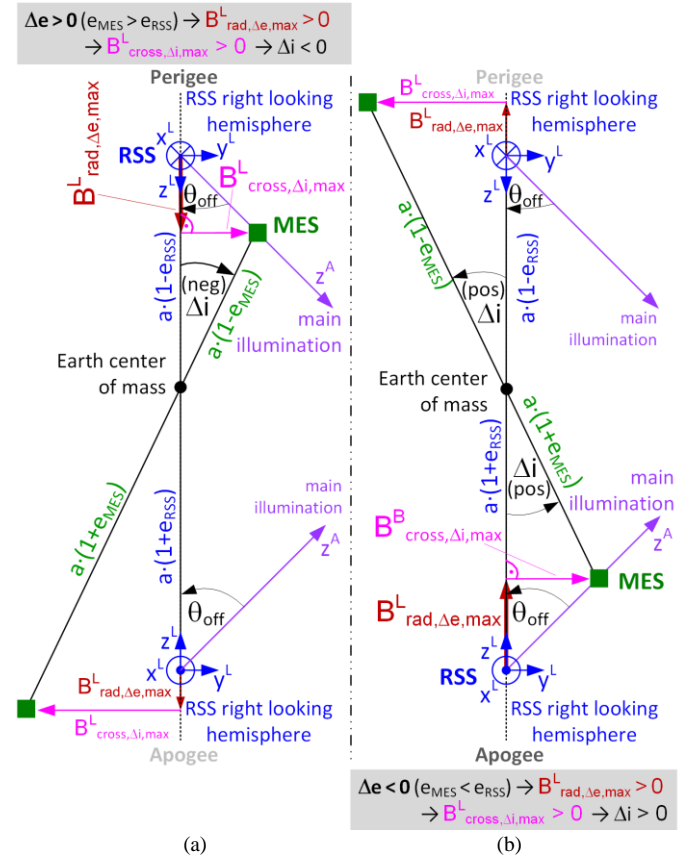
Fig. 24. Determination whether the antenna pattern measurement at a fixed azimuthal angle needs to be either around perigee or apogee. Right looking system. (a) For a positive eccentricity difference *Δe*, the measurement needs to be around perigee and the inclination difference *Δi* is required to be negative. (b) For a negative eccentricity difference *Δe*, apogee measurement is required together with a positive inclination difference *Δi*. The main illumination always points obliquely downward toward the Earth's surface.

In Fig. 24 (a) on the left, the eccentricity difference *Δe* is positive and thus the radial baseline is positive at perigee and negative at apogee. In order to position the measurement satellite into the main illumination direction of the radar

satellite, the cross-track baseline needs to be positive and the measurement needs to be carried out around perigee. At perigee, a positive maximum cross-track baseline in the *Local* system $B^L_{cross,\Delta i,max}$ is created by a negative inclination difference Δi, and therefore the negative sign has been introduced before the asin-function in (17).

The geometry for a negative eccentricity difference Δe is illustrated in Fig. 24 (b) on the left. The radial baseline is now negative at perigee and positive at apogee. In order to position the measurement satellite into the main illumination, a measurement around apogee is required, and the cross-track baseline $B^L_{cross,\Delta i,max}$ needs to be positive at apogee, which can be created by a positive inclination difference Δi. So, it can be summarized that the sign of Δi is required to be opposite to Δe.

For left looking geometry, equations (16) and (17) are applicable as well. For a positive Δe the radial baseline remains positive at the perigee but now a negative cross-track baseline $B^L_{cross,\Delta i,max}$ is required to position the measurement satellite to the left into the main radar satellite illumination, and thus Δi needs to be positive, which results from (17) since $\tan(\theta_{off})$ is negative for a negative θ_{off}. The analogue consideration shows that a negative eccentricity difference Δe requires apogee measurement for left looking as well as for right looking. Furthermore, the sign of the eccentricity difference Δe is determined by the sign of the azimuthal angle ξ in (16). An azimuthal angle $\xi < 0°$ requires measurement around perigee, and a measurement around apogee is required for $\xi > 0°$.

APPENDIX B: ROTATION OF RADAR SATELLITE

This appendix provides the equations to realize a mechanical rotation of the radar satellite by the azimuthal offset angle ξ_{off} around the *Antenna* system's z^A-axis by updating its attitude angles from yaw α, pitch β and roll γ angles into $\hat{\alpha}$, $\hat{\beta}$, and $\hat{\gamma}$. Using the rotational matrices introduced in Section III.B, the first line of (37) provides the transformation of the baseline vector from the *Local* into the *Antenna* system, i.e. from $\mathbf{B}^L$ into $\mathbf{B}^A$, by means of a separate rotation with the azimuthal offset angle ξ_{off}. By equalizing with the second line of (37), the desired $\hat{\alpha}$, $\hat{\beta}$, and $\hat{\gamma}$ can be derived that result in the same $\mathbf{B}^A$.

$$\mathbf{B}^A = {}^A D^{Ar}\left(\xi_{off}\right) \cdot {}^{Ar}D^B\left(\theta_{off}\right) \cdot {}^B D^L\left(\alpha,\beta,\gamma\right) \cdot \mathbf{B}^L$$
$$\mathbf{B}^A = \qquad\qquad {}^{Ar}D^B\left(\theta_{off}\right) \cdot {}^B D^L\left(\hat{\alpha},\hat{\beta},\hat{\gamma}\right) \cdot \mathbf{B}^L \qquad (37)$$

For $\hat{\beta}$, the following unambiguous equation can be derived:

$$\hat{\beta} = \operatorname{asin}\left(\cos\xi_{off} \cdot \sin\beta - \sin\xi_{off} \cdot \cos\beta \cdot \left(\cos\theta_{off} \cdot \sin\gamma - \sin\theta_{off} \cdot \cos\gamma\right)\right) \quad (38)$$

For $\hat{\gamma}$, two equations were derived, each with two possible solutions, and $\hat{\gamma}$ can be estimated by identifying the angle that resolves both equations.

$$\cos\hat{\gamma} = \left[\cos\beta \cdot \left(\sin\theta_{off} \cdot \sin\gamma + \cos\theta_{off} \cdot \cos\gamma\right) \cdot \cos\theta_{off}\right] \cdot \left(\cos\hat{\beta}\right)^{-1}$$
$$-\left[\sin\xi_{off} \cdot \sin\theta_{off} \cdot \sin\beta \quad + \cos\xi_{off} \cdot \sin\theta_{off} \cdot \cos\beta \cdot \left(\cos\theta_{off} \cdot \sin\gamma - \sin\theta_{off} \cdot \cos\gamma\right)\right] \cdot \left(\cos\hat{\beta}\right)^{-1}$$
$$(39)$$
$$\sin\hat{\gamma} = \left[\cos\beta \cdot \left(\sin\theta_{off} \cdot \sin\gamma + \cos\theta_{off} \cdot \cos\gamma\right) \cdot \sin\theta_{off}\right] \cdot \left(\cos\hat{\beta}\right)^{-1}$$
$$+\left[\sin\xi_{off} \cdot \cos\theta_{off} \cdot \sin\beta + \cos\xi_{off} \cdot \cos\theta_{off} \cdot \cos\beta \cdot \left(\cos\theta_{off} \cdot \sin\gamma - \sin\theta_{off} \cdot \cos\gamma\right)\right] \cdot \left(\cos\hat{\beta}\right)^{-1}$$

The same holds for $\hat{\alpha}$. In the equation for $\sin\hat{\alpha}$, the previously calculated value for $\cos\hat{\alpha}$ has been included.

$$\cos\hat{\alpha} = \left[\cos\xi_{off} \cdot \cos\beta \cdot \cos\alpha\right] \cdot \left(\cos\hat{\beta}\right)^{-1}$$
$$+\left[\sin\xi_{off} \cdot \left(\sin\beta \cdot \cos\alpha \cdot \left(\cos\theta_{off} \cdot \sin\gamma - \sin\theta_{off} \cdot \cos\gamma\right) - \sin\alpha \cdot \left(\cos\theta_{off} \cdot \cos\gamma + \sin\theta_{off} \cdot \sin\gamma\right)\right)\right] \cdot \left(\cos\hat{\beta}\right)^{-1}$$
$$+\left[\sin\xi_{off} \cdot \left(\sin\beta \cdot \cos\alpha \cdot \left(\cos\theta_{off} \cdot \sin\gamma - \sin\theta_{off} \cdot \cos\gamma\right) - \sin\alpha \cdot \left(\cos\theta_{off} \cdot \cos\gamma + \sin\theta_{off} \cdot \sin\gamma\right)\right)\right] \cdot \left(\cos\hat{\beta}\right)^{-1}$$
$$(40)$$
$$\sin\hat{\alpha} = \left[\sin\alpha \cdot \left(\sin\theta_{off} \cdot \cos\gamma - \cos\theta_{off} \cdot \sin\gamma\right)\right] \cdot \left(\sin\theta_{off} \cdot \cos\hat{\gamma} - \cos\theta_{off} \cdot \sin\hat{\gamma}\right)^{-1}$$
$$+\left[\sin\hat{\beta} \cdot \cos\hat{\alpha} \cdot \left(\sin\theta_{off} \cdot \sin\hat{\gamma} + \cos\theta_{off} \cdot \cos\hat{\gamma}\right)\right] \cdot \left(\sin\theta_{off} \cdot \cos\hat{\gamma} - \cos\theta_{off} \cdot \sin\hat{\gamma}\right)^{-1}$$
$$-\left[\sin\beta \cdot \cos\alpha \cdot \left(\sin\theta_{off} \cdot \sin\gamma + \cos\theta_{off} \cdot \cos\gamma\right)\right] \cdot \left(\sin\theta_{off} \cdot \cos\hat{\gamma} - \cos\theta_{off} \cdot \sin\hat{\gamma}\right)^{-1}$$

For the high-level system concept and the azimuthal offset angles of Section V, TABLE IV provides the updated attitude angles $\hat{\alpha}$, $\hat{\beta}$, and $\hat{\gamma}$ for initial attitude angles of zero.

TABLE IV
Update of radar satellite attitude angles to set the azimuthal offset angle ξ_{off}.

ξ_{off}	yaw $\hat{\alpha}$	pitch $\hat{\beta}$	roll $\hat{\gamma}$
-15°	-12.55°	-8.28°	0.91°
-5°	-4.16°	-2.78°	0.10°
5°	4.16°	2.78°	0.10°
15°	12.55°	8.28°	0.91
25°	21.2°	13.6°	2.6°

APPENDIX C: EQUATIONS FOR $\Delta\Omega$ TRADE-OFF

This appendix derives the maximum difference of the measurement and radar satellites orbit altitude Δh_{max} as well as the minimum and maximum length of the baseline vector, d_{min} and d_{max}, respectively, as functions of the difference in the ascending nodes $\Delta\Omega$. With these approximated equations, a suitable value for $\Delta\Omega$ is obtained by trade-off in Section IV.C.

In good approximation, d_{min} is the length of the baseline vector $\mathbf{B}^L$ at the argument of latitudes $u = \pm 90°$ for the largest absolute of the azimuthal angle $|\xi|$. At these orbit positions, the along-track baseline $B^L_{along,\Delta e}$ and the cross-track baseline contribution $B^L_{cross,\Delta\Omega}$ are close to zero and with (11), (16), and for small eccentricities the absolute of the baseline vector $\mathbf{B}^L$ can be approximated to the third line of (41). The largest $|\xi|$ in the denominator of the second line results for $\xi_{cut} = \pm 90°$ from the assigned azimuthal offset angle $\xi_{off, \pm 90°}$. Thus, the maximum of $|\xi_{off,\pm 90°}|$ determines d_{min}.

$$\left|\mathbf{B}^L\left(u = \pm 90°\right)\right|$$
$$\approx \sqrt{\left(B^L_{rad,\Delta e,max}\right)^2 + \left(B^L_{cross,\Delta i,max}\right)^2} = \sqrt{\left(B^L_{rad,\Delta e,max}\right)^2 + \left(B^L_{rad,\Delta e,max}\right)^2 \cdot \tan^2\theta_{off}}$$
$$\approx a \cdot \Delta e \cdot \sqrt{1 + \tan^2\theta_{off}} \approx 0.5 \cdot a \cdot \sin i_{RSS} \cdot \sin\Delta\Omega \cdot \frac{1}{\tan|\xi|} \qquad (41)$$
$$d_{min}\Big|_{\xi_{cut} = \pm 90°} \approx 0.5 \cdot a \cdot \sin i_{RSS} \cdot \sin\Delta\Omega \cdot \frac{1}{\tan\left|\pm 90° + \xi_{off,\pm 90°}\right|}$$
$$\Rightarrow d_{min} \approx 0.5 \cdot a \cdot \sin i_{RSS} \cdot \sin\Delta\Omega \cdot \tan\left(\max\left[\xi_{off,+90°}, \xi_{off,-90°}\right]\right)$$

The approximated maximum distance d_{max} is found at the equator where the radial baseline $B^L_{rad,\Delta e}$ and the cross-track baseline contribution $B^L_{cross,\Delta i}$ are close to zero. With (8), (9), and (16), the second line in (42) can be derived for small eccentricities. The smallest ξ in the second line is 0°. Therefore, d_{max} is determined by the distinct azimuthal offset angle $\xi_{off,0°}$ as is shown in the last line of the equation.

$$\left|\mathbf{B^L}\left(u=0°\right)\right| \approx \left|\mathbf{B^L}\left(u=180°\right)\right| \approx \sqrt{\left(B^L_{along,\Delta e,max}\right)^2 + \left(B^L_{cross,\Delta\Omega,max}\right)^2}$$

$$\approx a\cdot\sin i_{RSS}\cdot\sin\Delta\Omega\cdot\sqrt{\left(\frac{\cos\theta_{off}}{\tan\xi}\right)^2 + 1} \qquad (42)$$

$$d_{max}\big|_{\xi_{cut}=0°} \approx a\cdot\sin i_{RSS}\cdot\sin\Delta\Omega\cdot\sqrt{\left(\frac{\cos\theta_{off}}{\tan\xi_{off,0°}}\right)^2 + 1}$$

The maximum difference in orbits altitudes Δh_{max} can be approximated by the radial baseline $B^L_{rad,\Delta e}$ at the argument of latitudes $u = \pm90°$, and for small eccentricities, it results to the second line in (43).

$$B^L_{rad,\Delta e,max}\left(u=\pm90°\right) \approx 0.5\cdot a\cdot\sin i_{RSS}\cdot\sin\Delta\Omega\cdot\cos\theta_{off}\cdot\frac{1}{\tan\left(\min\left[\left|\xi\right|\right]\right)}$$

$$\Delta h_{max}\big|_{\xi_{cut}=0°} \approx 0.5\cdot a\cdot\sin i_{RSS}\cdot\sin\Delta\Omega\cdot\cos\theta_{off}\cdot\frac{1}{\tan\left(\left|\xi_{off,0°}\right|\right)} \qquad (43)$$

References

[1] J. Mittermayer, M. Younis, R. Metzig, S. Wollstadt, J. M. Martinez, and A. Meta, "TerraSAR-X system performance characterization and verification," IEEE Trans. Geosci. Remote Sens., vol. 48, no. 2, pp. 660–676, Feb. 2010.

[2] J. Mittermayer, B. Schättler, and M. Younis, "TerraSAR-X Commissioning Phase Execution Summary", IEEE Trans. Geosci. Remote Sens., vol. 48, no. 2, pp. 649–659, Feb. 2010.

[3] M. Bachmann, M. Schwerdt, B. Bräutigam, „TerraSAR-X Antenna Calibration and Monitoring Based on Precise Antenna Model", IEEE Trans. Geosci. Remote Sens., vol. 48, no. 2, pp. 690–701, Feb. 2010.

[4] M. Schwerdt, B. Bräutigam, M. Bachmann, B. Döring, D. Schrank, J. Jueso Gonzalez, "Final TerraSAR-X Calibration Results Based on Novel Efficient Methods," IEEE Trans. Geosci. Remote Sens., vol. 48, no. 2, pp. 677–689, Feb. 2010.

[5] T. Wang, C. Ruf, B. Block, D. McKague, „Characterization of the Transmit Power and Antenna Pattern of the GPS Constellation for the CYGNSS Mission", Proc. of IGARSS 2018.

[6] T. Wang, C. Ruf, B. Block, A. O'Brien, „ Measuring GPS Transmit Antenna Pattern Using On-Orbit Receivers", Proc. of 2019 IEEE International Symposium on Antennas and Propagation and USNC-URSI Radio Science Meeting, 2019.

[7] T. Qiu, Y. Wang, J. Hong, K Xing, S. Du, J. Mu, "An In-Orbit Measurement Method for Elevation Antenna Pattern of MEO Synthetic Aperture Radar Based on Nano Calibration Satellite, Remote Sens. 2022, 14, 741.

[8] Y. Wang, J. Hong, "Potentials of SAR Calibration Satellite Network in Spaceborne SAR External Calibration", Proc. of EUSAR 2018.

[9] J. Mittermayer, G. Krieger, A. Bojarski, M. Zonno, M. Villano, M. Pinheiro, M. Bachmann, S. Buckreuss, A. Moreira, "MirrorSAR: An HRWS Add-On for Single-Pass Multi-Baseline SAR Interferometry," IEEE Trans. Geosci. Remote Sens., vol. 60, Digital Object Identifier 10.1109/TGRS.2021.3132384, 2022.

[10] A. Moreira, G. Krieger, and J. Mittermayer, "Satellite configuration for interferometric and/or tomographic remote sensing by means of synthetic aperture radar (SAR)", U.S. Patent 6 677 884 Jul. 1, 2002.

[11] R. Kahle, B. Schlepp, F. Meissner, M. Kirschner, and R. Kiehling, "The TerraSAR-X /TanDEM-X formation acquisition – From planning to realization," J. Astronautical Sci., vol. 59, pp. 564–584, 2012.

[12] S. D'Amico, O. Montenbruck, C. Arbinger, and H. Fiedler, "Formation flying concept for close remote sensing satellites," in Proc. 15th AAS/AIAA Space Flight Mech. Conf., Copper Mountain, CO, 2005, pp. 831–848.

[13] G. Krieger et al., "TanDEM-X: A satellite formation for high-resolution SAR interferometry," IEEE Trans. Geosci. Remote Sens., vol. 45, no. 11, pp. 3317–3341, Nov. 2007.

[14] M. Zink, A. Moreira, I. Hajnsek, P. Rizzoli, M. Bachmann, R. Kahle, T. Fritz, M. Huber, G. Krieger, M. Lachaise, M. Martone, E. Maurer, B. Wessel, "TanDEM-X: 10 Years of Formation Flying Bistatic SAR Interferometry," IEEE Journal of Selected Topics in Applied Earth Observations and Remote Sensing, Vol. 14, pp 3546-3565, 2021.

[15] M. Bachmann, T. Kraus, A. Bojarski, M. Schandri, J. Böer, T. Busche, J. Bueso-Bello, C. Grigorov, U. Steinbrecher, S. Buckreuss, G. Krieger, M. Zink, „The TanDEM-X Mission Phases - Ten Years of Bistatic Acquisition and Formation Planning, IEEE Journal of Selected Topics in Applied Earth Observations and Remote Sensing, Vol. 14, pp 3504-3518, 2021.

[16] D. Massonnet, J.-J. Martin, „Radar Interferometry Device", PCT WO 99/58997, 18.11.1999.

[17] C. Klüver, "Space Flight Dynamics", John Wiley & Sons, LCCN 2017042818, 2018.

[18] M. Skolnik, "Radar Handbook, Third Edition", Mc Graw Hill, ISBN 978-0-07-148547-0, pp 14.5, 2008.

[19] J. C. Curlander and R. McDonough, Synthetic Aperture Radar. New York: Wiley, 1991.

[20] J. Mittermayer, S. Wollstadt, P. Prats-Iraola, and R. Scheiber, "The TerraSAR-X staring spotlight mode concept," IEEE Trans. Geosci. Remote Sens., vol. 52, no. 6, pp. 3695–3706, Jun. 2014.

[21] J. Mittermayer, S. Wollstadt, P. Prats, P. López-Dekker, G. Krieger, A. Moreira: "Bidirectional SAR Imaging Mode", IEEE Trans. on Geosc. Remote Sens., vol. 51, no. 1, pp. 601-614, January, 2013.

[22] I. G. Cumming and F. H. Wong, Synthetic Aperture Radar Data. Boston, MA, USA: Artech House, 2005.

[23] J. Mittermayer, G. Krieger, and M. Villano, Verfahren zur Vermessung eines Antennendiagramms einer Antenne auf einem ersten Flugobjekt mittels eines zweiten Flugobjekts, German Patent Application Nr. 10 2023 112 705.5, filed May 15, 2023. Patent pending.

[24] K. Wakker, Fundamentals of Astrodynamics. Institutional Repository Library, Delft Universtiy of Technology, http://repository.tudelft.nl, page 652, equation 23.54, 2015.

[25] S. Huber, F. Queiroz de Almeida, M. Villano, M. Younis, G. Krieger, A. Moreira, "Tandem-L: A Technical Perspective on Future Spaceborne SAR Sensors for Earth Observation", IEEE TGRS, Vol. 56, No. 8, August 2018.

[26] D. Petrolati et al., "An Overview of the Copernicus ROSE-L SAR Instrument", Proc. of IGARSS 2023, Pasadena, USA, 2023.

[27] D. Giudici, P. Guccione, M. Manzoni, A. Monti Guarnieri, F. Rocca, "Compact and Free-Floating Satellite MIMO SAR Formations", IEEE TGRS, Vol. 60, DOI 10.1109/TGRS.2021.3062973 , 2021.

[28] A. Renga, M. D. Graziano, M. Grasso, A. Moccia, "Evaluation of design parameters for formation flying SAR", Proc. of EUSAR, 2021.

[29] D. Giudici et al., "Compact and Free-Floating Satellite MIMO SAR Formations", IEEE TGRS, 2021.

Josef Mittermayer received the Dipl.-Ing. (M.Sc.) degree in electrical engineering from the Technical University of Munich, Munich, Germany, in 1995, the M.Sc. degree in space system engineering from the Delft University of Technology, Delft, The Netherlands, in 2004, and the Ph.D. degree from the University of Siegen, Siegen, Germany, in 2000.

Since 1994 he is with the Microwaves and Radar Institute, German Aerospace Center (DLR), Oberpfaffenhofen, Germany. From 2002 to 2008 he worked in the TerraSAR-X project, from 2004 to 2008 also in the TerraSAR-X group leader position. Additionally, he was the project manager of *TerraSAR-X System Engineering and Calibration*, and was technically responsible for the TerraSAR-X commissioning phase. His scientific and engineering work includes the fields SAR processing, SAR system engineering, and SAR mode development. Currently, NewSpace and formations of small multistatic SAR satellites is a focus of his work. Apart from numerous conference papers and patents in the field of SAR, Dr. Mittermayer is author or co-author of more than 20 peer-reviewed journal papers.

Dr. Mittermayer and his colleagues were recipients of the IEEE Geoscience and Remote Sensing Society Transactions Prize Paper Award for a paper on air and spaceborne stripmap and ScanSAR processing in 1996. He was a recipient of the DLR Science Award in 2001 for his work on spotlight-SAR processing. In 2011, he was awarded with the DLR Science Semester for his contribution to the TerraSAR-X project. He and his colleagues were recipients of the DLR Science Award in 2023 for their work on a MirrorSAR extension to the HRWS mission proposal.

Gerhard Krieger (M'04-SM'09-F'13) received the Dipl.-Ing. (M.S.) and Dr.-Ing. (Ph.D.) (Hons.) degrees in electrical and communication engineering from the Technical University of Munich, Germany, in 1992 and 1999, respectively.

From 1992 to 1999, he was with the Ludwig Maximilians University, Munich, where he conducted multidisciplinary research on neuronal modeling and nonlinear information processing in biological and technical vision systems. Since 1999, he has been with the Microwaves and Radar Institute of the German Aerospace Center (DLR), Oberpfaffenhofen, Germany, where he started as a research associate developing signal processing algorithms for a novel forward-looking radar system employing digital beamforming on receive. From 2001 to 2007, he led the New SAR Missions Group which pioneered the development of advanced bistatic and multistatic radar systems, such as TanDEM-X, as well as innovative multichannel SAR techniques and algorithms for high-resolution wide-swath SAR imaging. Since 2008, he has been the Head of the Radar Concepts Department which currently hosts about 60 scientists focusing on new SAR techniques, missions and applications. He has been serving as Mission Engineer for TanDEM-X and he made also major contributions to the development of the Tandem-L mission concept, where he led the Phase-0 and Phase-A studies. Since 2019, he holds also a professorship at the Friedrich-Alexander-University Erlangen, Germany, and he is author or co-author of more than 100 peer-reviewed journal papers, 9 invited book chapters, about 500 conference papers, and more than 30 patents.

Prof. Krieger has been an Associate Editor for the IEEE Transactions on Geoscience and Remote Sensing since 2012. In 2014 and 2024, he served as the Technical Program Chair for the European Conference on Synthetic Aperture Radar and in 2014 also as a Guest Editor for the IEEE Journal of Selected Topics in Applied Earth Observations and Remote Sensing. He received several national and international awards, including two Best Paper Awards at the European Conference on Synthetic Aperture Radar, two Transactions Prize Paper Awards of the IEEE Geoscience and Remote Sensing Society, and the W.R.G. Baker Prize Paper Award from the IEEE Board of Directors.

Michelangelo Villano (Senior Member, IEEE) received the B.Sc. and M.Sc. degrees (Hons.) in telecommunication engineering from the Sapienza University of Rome, Rome, Italy, in 2006 and 2008, respectively, and the Ph.D. degree (Hons.) in electrical engineering and information technology from the Karlsruhe Institute of Technology, Karlsruhe, Germany, in 2016.

From 2008 to 2009, he was a Young Graduate Trainee with the European Space Research and Technology Center, European Space Agency, Noordwijk, The Netherlands, where he developed processing algorithms for ice sounding radar. Since 2009, he has been with the German Aerospace Center (DLR), Microwaves and Radar Institute, Wessling, Germany, where he developed, among others, the staggered synthetic aperture radar (SAR) acquisition mode that allows imaging a wide swath with high resolution through continuous variation of the pulse repetition interval. Since 2019, he has been the Head of the NewSpace SAR Research Group, where he leads the development of cost-effective and multi-static SAR concepts for frequent and enhanced Earth monitoring. In 2017, he was a Visiting Research Scientist with the Communications, Tracking, and Radar Division, NASA Jet Propulsion Laboratory, Pasadena, CA, USA, where he adapted the staggered SAR mode to the NASA-ISRO SAR (NISAR) mission, for which staggered SAR is the baseline acquisition mode. Since 2019, he has also been a Lecturer with Ulm University, Ulm, Germany. He has authored or coauthored 40 peer-review journal papers, a book chapter, and over 100 articles in international conference proceedings. He holds 11 patents in the field of SAR.

Dr. Villano was a recipient of the First Place Student Paper Award at the European Conference on Synthetic Aperture Radar (EUSAR), Berlin, Germany, in 2014, the IEEE Geoscience and Remote Sensing Society Letters Prize Paper Award in 2015 and 2017, the Student Paper Award at the Asia–Pacific Conference on Synthetic Aperture Radar, Marina Bay Sands, Singapore, in 2015, the DLR Science Award in 2016 and 2023, the Award as Young Scientist of the Foundation Werner von Siemens Ring in 2017, the ITG Dissertation Award in 2017, and the Best Paper Award at the German Microwave Conference 2019. In 2022, he was awarded a Starting Grant by the European Research Council (ERC). He is co-chair of the Working Group on "Active Microwave: Radar and SAR" of the IEEE Geoscience and Remote Sensing Society's Technical Committee on Instrumentation and Future Technologies. He serves as an Associate Editor for the IEEE Transactions of Geoscience and Remote Sensing. He served as a Technical Program Chair for the EUSAR 2024.